UCLA
UCLA Previously Published Works

Title
Surface Structure of Co3O4 (111) under Reactive Gas-Phase Environments

Authors
Yan, George
Sautet, Philippe

Supplemental Material
https://escholarship.org/uc/item/56n0k4qz#supplemental

Peer reviewed

The Surface Structure of Co_3O_4(111) under Reactive Gas Phase Environments

George Yan[1], Philippe Sautet[1, 2, *]

[1] Department of Chemical and Biomolecular Engineering, University of California, Los Angeles, Los Angeles, California 90095, United States
[2] Department of Chemistry and Biochemistry, University of California, Los Angeles, Los Angeles, California 90095, United States

Abstract:

In this work, we thoroughly examined the structure of the Co_3O_4(111) surface in oxidative and reductive conditions, i.e. in equilibrium with realistic pressures of O_2/H_2O and H_2/H_2O, using density functional theory with self-interaction and dispersion corrections. We found that this surface is, in fact, hydroxylated under most reaction conditions, and that subjecting the surface to H_2 increases surface Co^{2+} concentration. Large structural distortions facilitate the reduction and stabilization of the Co-rich termination. At 423 K, hydroxylation readily occurs on both the O-rich and Co-rich surfaces even at water pressure as low as 10^{-15} bar, and non-dissociated water molecules appear on the O-rich surface when water pressure is above ~10^{-11} bar. Our approach showed good agreement with hybrid functional calculations and vibrational spectroscopy experiments. Under most catalytic conditions, where water is present as a reactant, product, or impurity, we predict that the Co_3O_4(111) surface will be hydroxylated. Hydroxyls groups and structural distortions undoubtedly play large roles in shaping the surface's catalytic properties and interaction with supported structures. The results of the study show the necessity of the inclusion of hydroxylation and surface Co concentration in computational studies of Co_3O_4 and provide surface structures under various conditions to aid in future studies on structure and catalytic reactivity of Co_3O_4(111) used as a support or as an active phase.

Keywords: Cobalt (II, III) oxide, DFT+U, hydroxylation, surface structure, surface stability

1. Introduction

Cobalt(II,III) oxide, Co_3O_4, is a versatile metal oxide capable of being both a catalyst support for single noble metal (NM) atoms, metal clusters, and a catalyst itself.[1,2] The catalytic properties of Co_3O_4 have been studied extensively. In thermal catalysis, Co_3O_4 is found to be active for low temperature CO/hydrocarbon oxidation, NO_x reduction, N_2O decomposition, and selective catalytic reduction of NO with NH_3.[1,3] Most groups have attributed the material's extraordinary oxidation activity to its reducibility. On the other hand, NO reduction by H_2 can be performed over various NM_1/Co_3O_4 catalysts, where Co_3O_4 acts as the support.[4] One promising application of the (111) surface is the oxidative dehydrogenation (ODH) of alkanes.[5,6] The (111) surface has recently been shown to have good selectivity for ethane ODH against combustion.[7]

Co_3O_4 has the normal spinel structure and an indirect band gap. Co^{2+} in tetrahedral (T_d) sites are in the quadruplet spin state while Co^{3+} in octahedral (O_h) sites are in the singlet spin state.[8] Co^{2+} ions aligned on the same (111) plane have the same spin direction, and these (111) planes are antiferromagnetically aligned in the bulk.[9] Experimentally, Co_3O_4 particles calcined at 673 K expose (100), (110), and (111) surfaces in similar portions.[10] In the case of the (111) surface, it is polar and can be terminated by Co in tetrahedral sites (Co-T_d), octahedral sites (Co-O_h), O^{2-}, or a mix of the three for a total of six unique bulk-truncated terminations (Figure 1). Thin films exposing O^{2-} and Co-T_d relax inwards to compensate for the surface dipole.[11,12] The relative stability of bulk-truncated low miller index Co_3O_4 surfaces have been examined by various studies under purely oxygen-containing environments.[10,13–15]
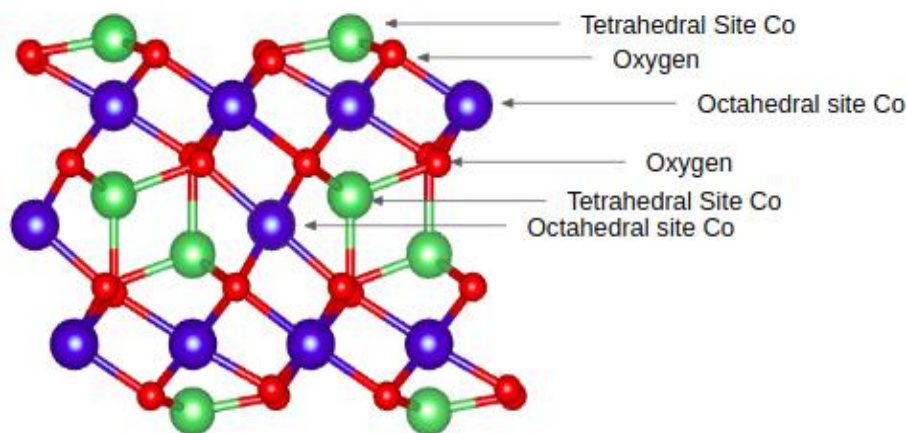
Figure 1. Side view of Co_3O_4 through the [111] direction. From truncating the Co_3O_4 bulk, a total of six possible terminations of the (111) surface can be made. This surface is a type III surface by Tasker's definitions, where the group of the six labeled layers is stoichiometric when stacked but has a net dipole in the z-direction

Experimental characterization of the Co_3O_4 (111) surface is a challenging task. Busca et al. obtained IR spectra of the surface after diluting the sample with KBr and activating under vacuum.[16] Vibrational modes in the fingerprint region (<1000 cm^{-1}) were present, but the overall IR transmission window is severely limited.[16] High temperature evacuation or H_2 reduction were found to widen this window, but carry the risk of reducing the Co_3O_4 sample to CoO. To mitigate this problem, alternative characterization techniques can be used, but they are generally limited to ultra-high vacuum (UHV).[17] Although x-ray photoelectron spectroscopy (XPS) can now be performed at ambient pressures, it is still difficult to identify types of surface O because OH$^-$, CO_3^{2-}, and defective O all have similar O 2p binding energy.[2,17–20] Petitto et al. used XPS and high-resolution electron energy loss spectroscopy (HREELS) to study surface OH created on (111)-terminated single Co_3O_4 crystals after annealing in H_2O.[21] Schwarz et al. probed Co_3O_4(111) epitaxial films using XPS and infrared reflection absorption spectroscopy (IRAS) after exposing them first to D_2O or CO.[22,23] To summarize, experimental characterization of the Co_3O_4(111) surface can only provide a limited view of the surface at low pressures. These

difficulties highlight the importance of theoretical studies for understanding surface structure, especially outside the limits of experimental characterization.

Although many computational studies have been performed on the $Co_3O_4(111)$ surface using density functional theory (DFT), they generally lack three considerations. First, only a few studies regard the magnetic structure, even when it was shown that inconsistent magnetic coupling induces errors in calculated energy.[24–26] Second, mechanistic studies of reactions on the (111) surface generally do not consider the role of hydroxyls.[5–7] Low pressure H_2O/D_2O exposure experiments have shown that hydroxyls are stable on the surface up to 570 K.[23] Further, H_2 was also shown to dissociate easily over the (111) termination.[27] Therefore, any H_2O or H_2 impurity in the gas environment will likely produce hydroxyls. Third, the electronic effects of surface reduction are not addressed in most studies. Early studies used generalized gradient approximation (GGA) exchange correlation functionals but did not include any self-interaction error correction for Co 3d electrons.[13,28] Conventional DFT predicts a bulk band gap that is too narrow.[9,29] Only a few studies have addressed electron localization upon reduction.[24–26]

The Co^{2+} and O^{2-} terminated surface is the most often used as the active site structure for the (111) termination.[5–7] In this study, we seek to provide insight into the structure of this surface under various reaction environments. We examine the structure of the surface in equilibrium with O_2, H_2O, and H_2 to address surface hydroxylation, vacancy formation, and possible change of the Co concentration, while taking a rigorous approach and minding both the bulk magnetic structure and electronic effects that occur through surface modifications.

2.   Computational details

2.1   Computational methods

Density functional theory (DFT) calculations were performed using the Vienna ab-initio simulation package (VASP), version 5.4.1.[30–32] Exchange-correlation energy was calculated using the Perdew-Burke-Erzenhof (PBE) functional.[33] Spin polarization was applied in all calculations unless otherwise specified. Since PBE does not account for van der Waals (vdW) forces, the dDsC dispersion-correction method was used.[34,35] The projector-augmented-wave (PAW) method was used to describe the core electrons.[36] The one-electron wavefunctions are developed on a basis set of plane waves with a 450 eV energy cutoff. To correct for the large self-interaction error of the $3d$ electrons of Co, a Hubbard-like repulsion term was added using Dudarev's approach (DFT+U), with $U_{eff} = U - J = 3.5$ eV.[37] This value of U_{eff} is consistent with those found in literature as a value that properly describes the energy of formation of Co_3O_4 from CoO.[38] Due to the controversy on choosing the appropriate U_{eff}, calculations using $U_{eff} = 2.0$ eV were also performed starting from $U_{eff} = 3.5$ eV geometry. Single point calculations using the Heyd-Scuseria-Ernzerhof functional with dispersion (HSE06+dDsC) were also performed using geometry and charge density obtained from $U_{eff} = 3.5$ eV as benchmarks for vacancy formation energies.[39,40] Previously, we benchmarked the energy of water adsorption on 11-layered Co-T_d-terminated slabs at the PBE+U+dDsC level ($U_{eff}=3.5$ eV), against HSE06+dDsC. We found that water is under bound by 0.15 eV/H_2O when using PBE+U+dDsC. This same correction was applied to all water-adsorbed structures to construct the 1-D and 2-D surface stability diagrams in this work.

Since Co^{2+} ions in Co_3O_4 are known to have antiferromagnetic ordering in the bulk, while Co^{3+} ions have no magnetic moment, careful considerations were taken to ensure that the bulk-

like section of the slab retains the correct Co^{2+} magnetic ordering and spin state. Electron localization or delocalization were also properly ensured on the modified surface, so that no electrons were spuriously added to the other side of the slab. Specifically, the occupancy matrix control technique developed by Allen and Watson was used, where a spin-polarized VASP WAVECAR file containing desirable Co 3d projected electron occupations was generated and used as the starting guess for the system.[41]

The surface structures considered in this work were compared to each other by their surface Gibbs free energy[42,43], under a given temperature and a set of gas pressures (Section S1). DFT energies used to develop the surface stability diagrams were all computed from structures in (2×2) supercells (a, b, c axes shown on Figure 2 a and d) to ensure proper calculation of vdW contributions to electronic energy with dDsC. At PBE+U+dDsC level, assessing the adsorption energy of water in a (1×1) cell induces an error within 0.025 eV/H_2O. The outermost layer of O and Co atoms were displaced in the frequency calculations (Table S13). For a (2×2) slab (a = b = 11.4 Å, γ = 120°), the Brillouin zone was sampled using a $3 \times 3 \times 1$ Monkhorst-Pack mesh.[44] Electronic energy difference between steps in each self-consistent field (SCF) cycle were converged to 10^{-6} eV, and atomic positions were converged until the forces on unconstrained atoms are less than 0.02 eV/$Å^{-1}$. A (1×1) cell was used for HSE06+dDsC calculations, with a 3 $\times 3 \times 1$ Monkhorst-Pack mesh. At PBE+U+dDsC level, reducing the k-point mesh from $6 \times 6 \times 1$ to $3 \times 3 \times 1$ in a (1×1) cell only increases the total energy by <0.1 meV/atom. The lattice parameter and the atomic positions of the bulk cell were relaxed simultaneously. Structural and electron density visualizations were performed using the VESTA program.[45] Vibrational frequencies were calculated using finite differences with a step size of 0.015 Å. The calculated

v(OH) and v(OD) modes were rescaled by factors of 0.9789 and 0.9918 respectively; these factors were calculated using the same scheme as that specified by Freund, Sauer et al.[46]

2.2 Bulk and surface models

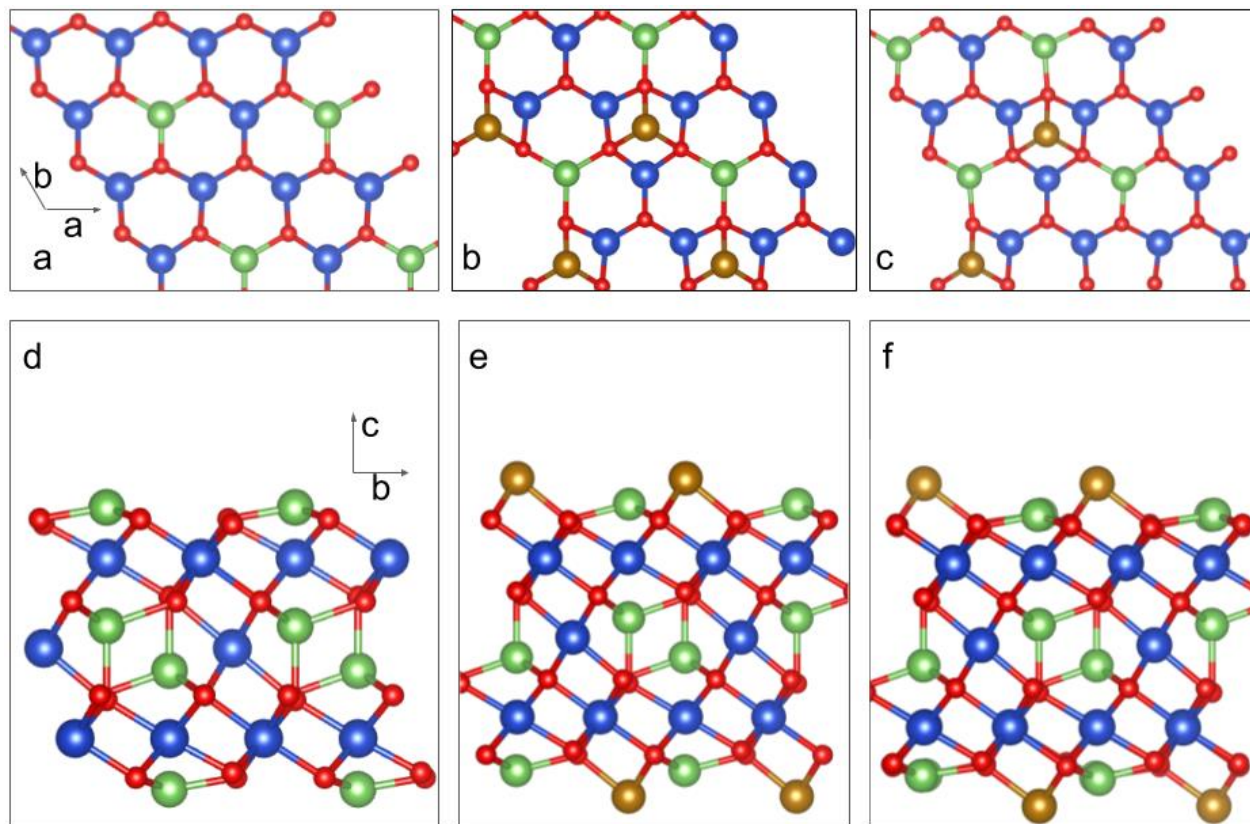**Figure 2.** Top (a, b, c, through the c axis) and side (d, e, f, through the a axis) views of (2x2) cells (area 1.13 nm^2) of the three bare $Co_3O_4(111)$ terminations considered in this work, containing (red) O, (green) Co-T_d and (blue) Co-O_h and additional surface Co (gold). a, d: O-rich termination, $(Co^{Td})_x$, has formula $Co_{44}O_{64}$, containing four exposed Co in C_{3v} sites on each surface, belonging to bulk T_d sites in the bulk. b, e: Co-rich termination, $(Co^{Oh}Co^{Td})_x$, has formula $Co_{52}O_{64}$, containing eight exposed Co in C_{3v} sites on each surface; four originally at bulk T_d sites and four originally at bulk O_h sites. c, f: stoichiometric termination, $(Co^{Oh}_{0.5}Co^{Td})_x$, has formula $Co_{48}O_{64}$, containing six exposed C_{3v} Co on each surface; two originally at bulk O_h sites and four at bulk T_d sites.

A cubic $Co_{24}O_{32}$ cell was used to model the Co_3O_4 bulk. The lattice parameter was found to be 8.06 Å, which matches the experimental lattice parameter, 8.08 Å.[47] A magnetic moment of 2.64 μ_B was found on the Co^{2+} ions in the bulk, consistent with values obtained by Selloni et al.,

but lower than the 3.26 μ_B measured by Roth.[8,9] As previously mentioned, Co_3O_4(111) is a Tasker type III polar surface with six different bulk-truncated terminations. To simulate the surface, three terminations, previously proposed by Zasada et al., were chosen (Figure 2).[48] $(Co^{Td})_x$ and $(Co^{Oh}Co^{Td})_x$ were cut directly from the bulk and are oxygen-rich and cobalt-rich respectively, while $(Co^{Oh}_{0.5}Co^{Td})_x$ is stoichiometric.[48] A symmetric 11-layer slab was used to model $(Co^{Td})_x$, and symmetric 13 layer slabs were used to model $(Co^{Oh}Co^{Td})_x$ and $(Co^{Oh}_{0.5}Co^{Td})_x$. In a (2×2) cell, they have formulas $Co_{44}O_{64}$, $Co_{52}O_{64}$ and $Co_{48}O_{64}$, containing 3.56, 7.11, and 5.33 Co/nm^2 respectively. The $(Co^{Td})_x$ surface contains two unique types of surface O: those directly adjacent to surface Co^{Td} (Figure 2a, red O bonded to 2 blue Co and 1 green Co) and those in isolation (Figure 2a, bonded to 3 blue Co). To simulate 5.33 Co/nm^2, Co is added to three-fold adjacent O sites, generating another category of O bonded to both Co^{Td} and Co^{Oh} (Figure 2b, red O bonded to 2 blue Co, 1 green Co, and 1 gold Co). Finally, when all the three-fold O sites are occupied on the surface by Co at 7.11 Co/nm^2, two types of O exist on the surface: isolated O and those between Co^{Td} and Co^{Oh}.

The antiferromagnetic alignment of surface Co ions on the $(Co^{Oh}_{0.5}Co^{Td})_x$ termination was challenging to keep consistent; therefore, they were kept ferromagnetic and shifted by a constant correction per unit cell (see Figure S12). At least 15 Å of vacuum was used to prevent interactions between slabs in the z direction. For a given slab calculation, the five innermost layers were fixed to their bulk positions and all other atoms were relaxed. Adsorption of atoms and molecules were performed on only one side of the slab to prevent surface-surface interactions through the slab. Dipole corrections were applied in all slab calculations. H adsorption, H_2O adsorption, and oxygen vacancy formation were considered separately on all three surfaces, and the combination of up to 1.78 H_2/nm^2 (up to 4 H added per unit cell) and 2.78

H_2O/nm^2 (up to 3 H_2O added per unit cell) on the $(Co^{Td})_x$ termination as a simplified case of H/H_2O co-adsorption. At given set of temperature and partial pressure, surfaces are compared to each other through approximate surface energy (see section S1).

3.   Results and discussion

3.1   Co$_3$O$_4$(111) surface stability diagrams

For oxidative reactions, we consider the surface to be in equilibrium with O_2 and H_2O. The surface stability diagram under realistic O_2 and H_2O chemical potentials ($\Delta\mu_{H2O} > -2.5$ eV, $\Delta\mu_O > -2.5$ eV) is shown below:
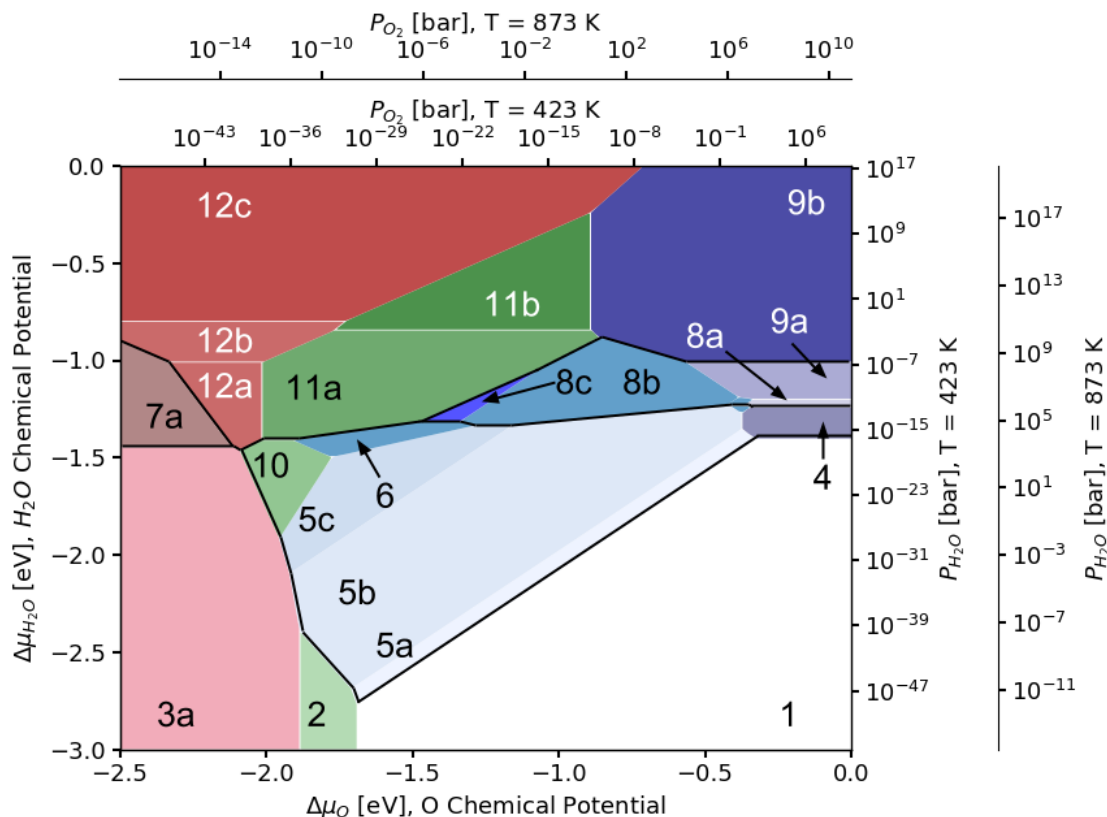
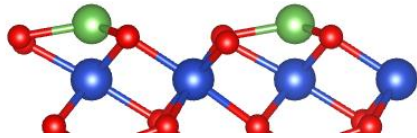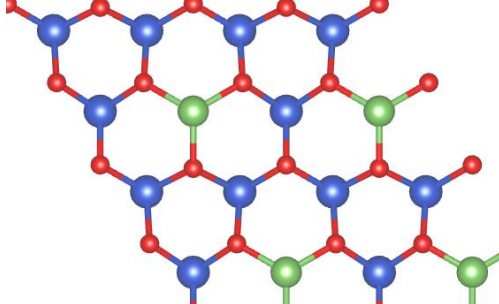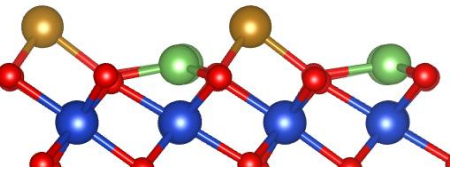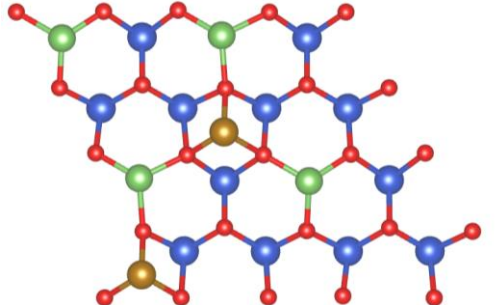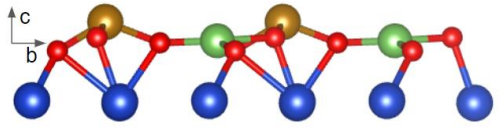**Figure 3.** Surface stability diagram showing the most stable surface structure as a function of O_2 and H_2O chemical potential and equivalent ox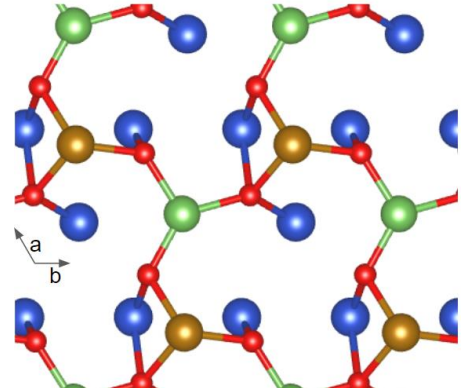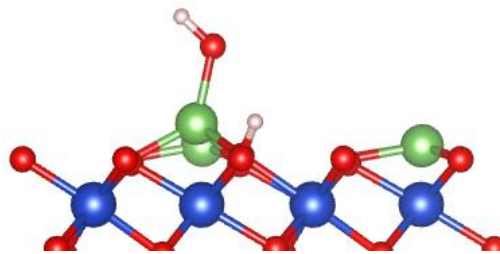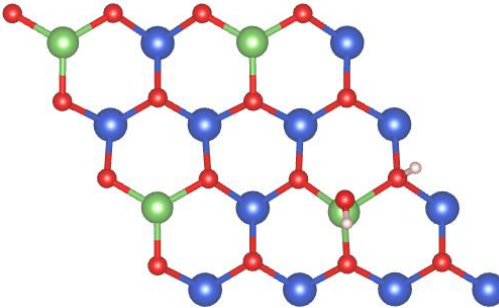ygen/water pressure at 423 K and 873 K. Regions are classified in 3 ways. I) By surface Co concentration: blue/grey/white: 3.56 Co/nm^2; green: 5.33 Co/nm^2, and red/brown: 7.11 Co/nm^2.   II) By general appearance of surface hydroxylation: bottom bold line separates non-hydroxylated regions and hydroxylated regions, middle bold line (only the segment running through the blue regions, or when $\Delta\mu_O > -1.5$ eV) separates isolated hydroxyls and $Co(H_2O)_3$ (hereby referred to as "triaqua") surface complexes (with eventually additional OH groups), and top bold line separates isolated triaqua surface complexes and large OH/H_2O structures. III) By specific numbered structure (see Table 1 for descriptions, Figure 2 and Table 2 for representative geometries, and Table S10 for all geometries).

Table 1. Description of the specific types of surface structures observed in Figure 3 and 5

Label(s) on Figure 3 and/or Figure 5	Termination, coverage, and appearance
1	Bare $(Co^{Td})_x$ surface
2	Bare $(Co^{Oh}_{0.5}Co^{Td})_x$ surface
3 a, b	$(Co^{Oh}Co^{Td})_x$ surface with: a) 3.56 O_{vac}/nm^2 and b) 7.11 O_{vac}/nm^2
4	$(Co^{Td})_x$ with 1.78 OH/nm^2, appearing as 1 dissociated H_2O
5 a-c	$(Co^{Td})_x$ with: a) 0.89, b) 1.78, c) 2.67 OH/nm^2, appearing as adsorbed H
6	$(Co^{Td})_x$ with 5.33 OH/nm^2, appearing as 4 adsorbed H and 1 dissociated H_2O
7 a-e	$(Co^{Oh}Co^{Td})_x$ with: a) 7.11 OH/nm^2, b) 8.00 OH/nm^2, c) 8.89 OH/nm^2, d) 9.78 OH/nm^2, e) 10.67 OH/nm^2, appearing as dissociated H_2
8 a-c	$(Co^{Td})_x$ with: a) 0 OH/nm^2 and 2.67 H_2O/nm^2 b) 2.67 OH/nm^2 and 2.67 H_2O/nm^2, c) 2.67 H_2O/nm^2 and 3.56 OH/nm^2, appearing as one triaqua surface complex eventually surrounded by adsorbed H
9 a, b	$(Co^{Td})_x$ with: a) 3.56 H_2O/nm^2, 3.56 OH/nm^2 and b) 5.33 OH/nm^2, 4.44 H_2O/nm^2, each containing one triaqua surface complex and H-bonded OH/H_2O chain. The triaqua complex is incorporated into the chain in structure 9b
10	$(Co^{Oh}_{0.5}Co^{Td})_x$ with 3.56 OH/nm^2, appearing as dissociated H_2O
11 a, b	$(Co^{Oh}_{0.5}Co^{Td})_x$ with: a) 8.89 OH/nm^2 and 0.89 H_2O/nm^2, b) 10.89 OH/nm^2 and 1.78 H_2O/nm^2, appearing as dissociated and molecular H_2O
12 a-c	$(Co^{Oh}Co^{Td})_x$ with: a) 8.89 OH/nm^2, 0.89 H_2O/nm^2, b) 7.11 OH/nm^2 and 5.33 H_2O/nm^2, c) 7.11 OH/nm^2 and 7.11 H_2O/nm^2, appearing as dissociated and molecular H_2O linked by H bonds.

Table 2. Side (through the a axis) and top (through the c axis) views of representative structures in regions 1-12 on the surface stability diagram (see Table 1, Figure 3, and Figure 5). 4 and 9b are adapted from ref [49].

Number	Geometry, side view, through a axis	Geometry, top view, through c axis
(1)		
(2)		
(3)		
(4)		

(10)		
(11a)		
(12c)		
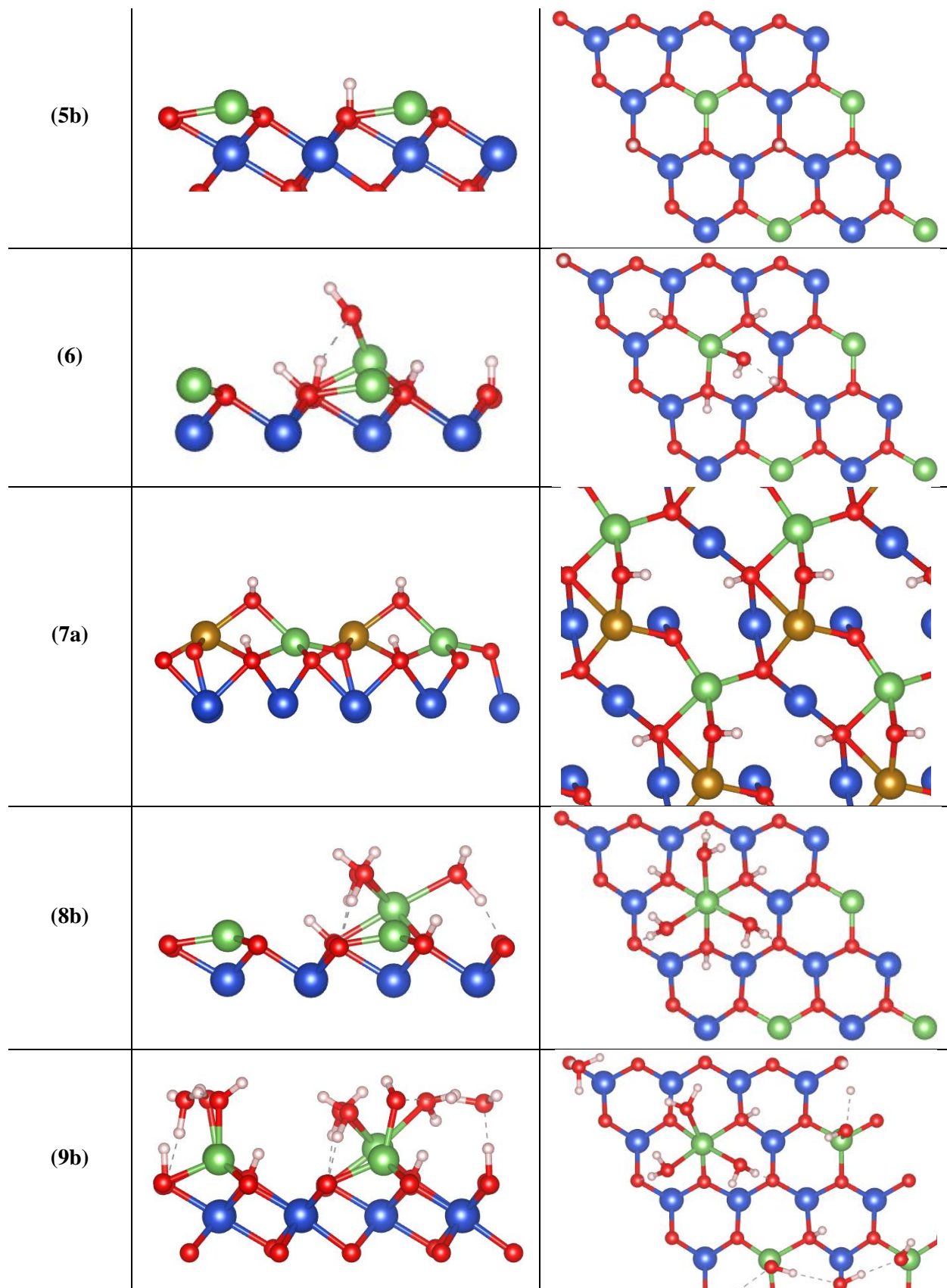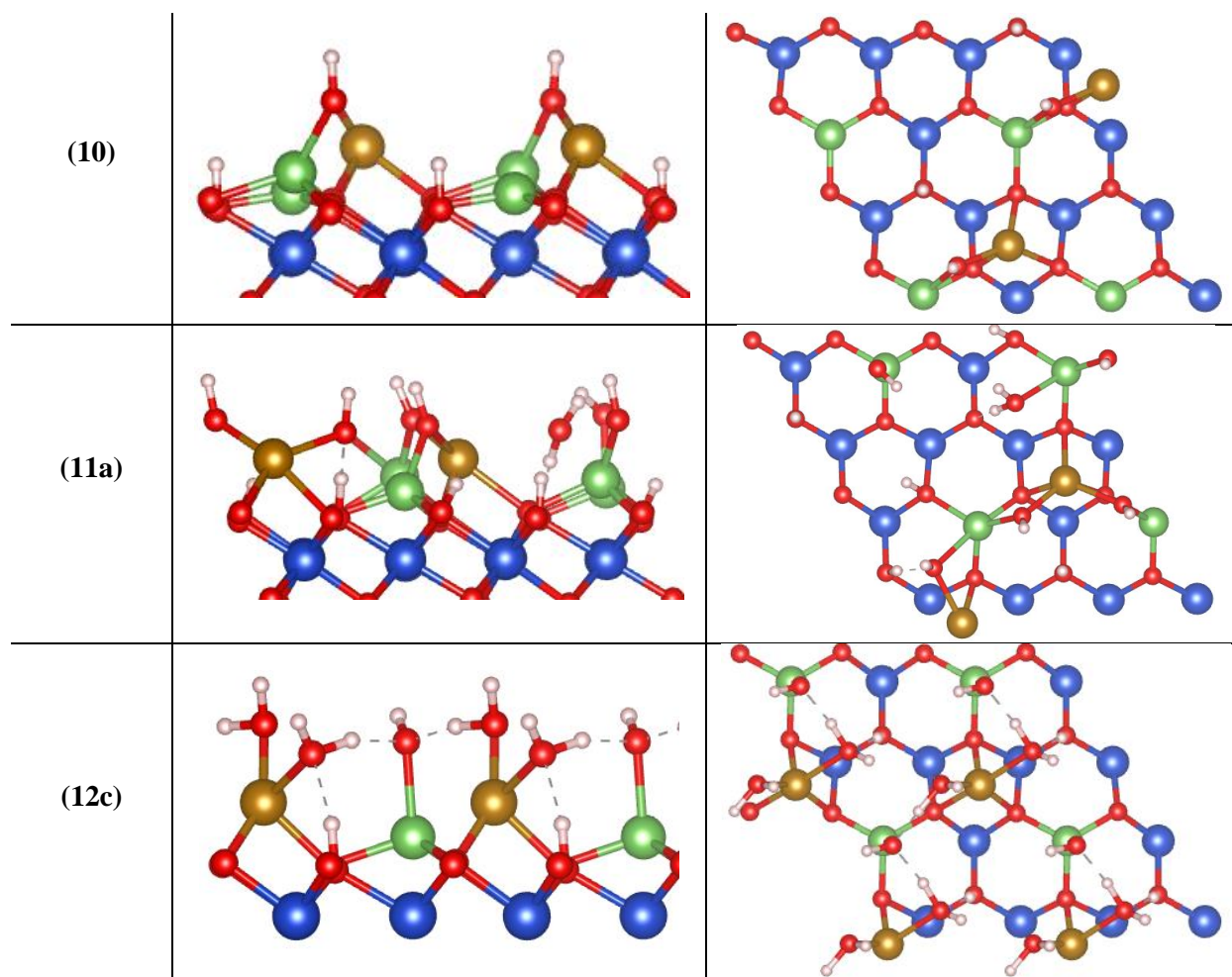
While in equilibrium with O_2 and H_2O, the surface stability diagram is dominated by the $(Co^{Td})_x$ termination. Only considering the $(Co^{Td})_x$ regions, the diagram can be drawn into four sections based on the type of surface hydroxyls present. It should be noted that the structures listed in Table 1 are representatives of the various macroscopic regions on the stability diagram; it is possible that there are more stable isomers. These four regions are separated by bold black lines (Figure 3). The lowest line separates the non-hydroxylated regions below the line from strong surface hydroxyl groups. Under H_2O and O_2 pressure, these regions can be interpreted as the equilibrated states of H_2O adsorption on surface vacancies. The coverage of isolated OH should be 2~4 OH/nm^2 (Table 1, Table 2 and Table S1). As mentioned in section 2.2, two types

of O exist on the $(Co^{Td})_x$ surface, ones adjacent to surface Co^{Td}, coordinated to the surface Co^{Td} and to subsurface Co^{Oh}, and ones in isolation, coordinated to 3 subsurface Co^{Oh}. It is more favorable to populate isolated O first. The line second-to-the-bottom, running across at roughly -1.3 eV, separates the isolated OH region to the one containing triaqua surface complexes, surrounded by OH groups coming from adsorbed H atoms. Structure 8b (Table 2, row 6) can serve as a representative for such OH-surrounded triaqua surface complexes, where one surface Co^{Td} is coordinated to three molecular H_2O and adjacent to three surface OH. Finally, the upper line, running across at roughly -1.1 eV, divides the triaqua surface complex-containing region below and the fully wetted region, containing extended H-bonded OH/H_2O structures. On the other hand, the diagram can also be divided by surface Co concentration. Regions in shades of blue/grey and white are Co poor (3.56 Co/nm^2), regions in green are stoichiometric (5.33 Co/nm^2), and regions in red and brown are Co-rich (7.11 Co/nm^2). As expected, surface Co concentration increases as $\Delta\mu_O$ decreases through all the major zones, i.e. when the gas environment shifts towards O poor conditions.
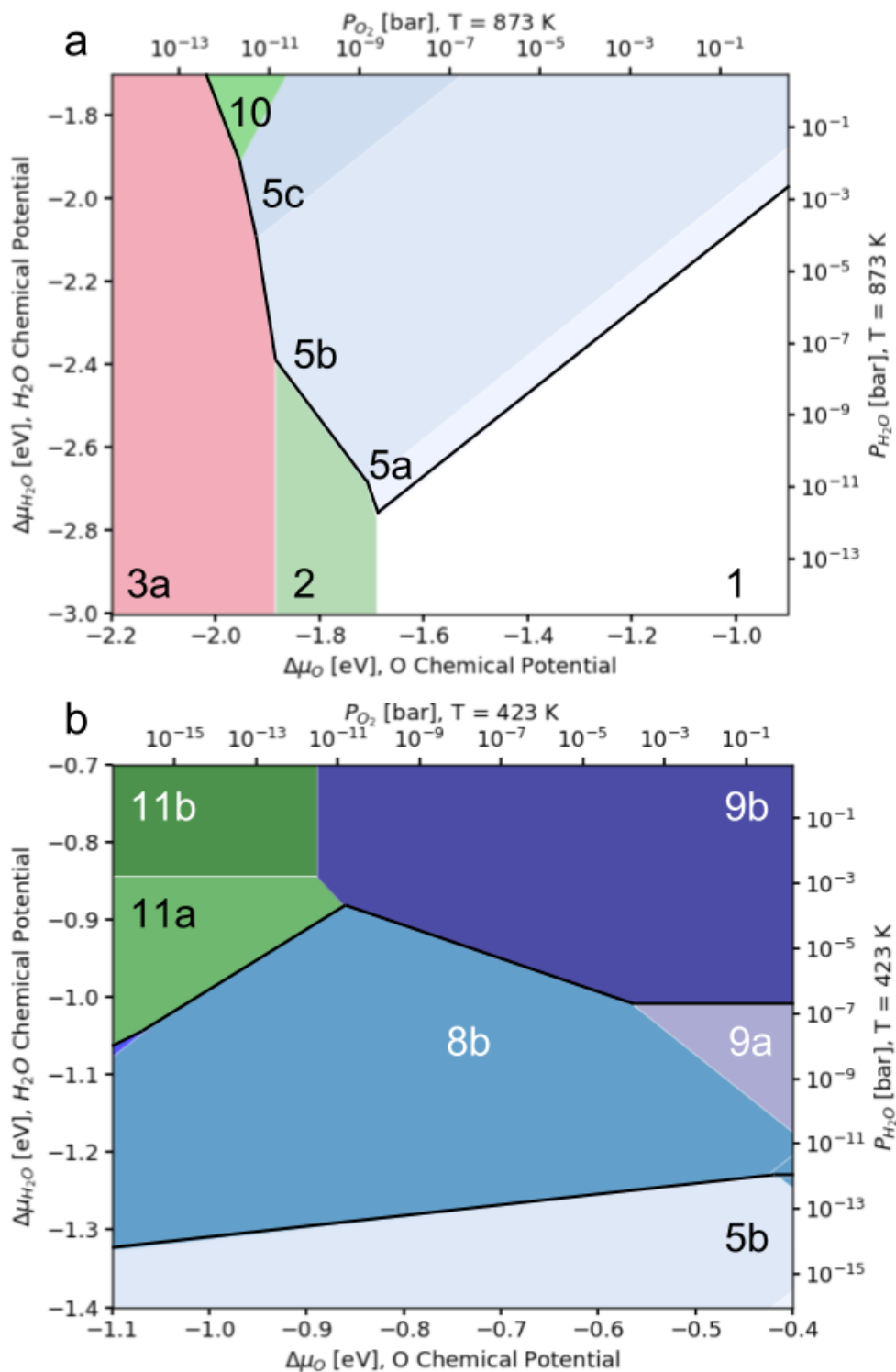
Figure 4. Portions of Figure 3 showing the H_2O/O_2 surface stability diagram under realistic pressures at (top) 423 K and (bottom) 873 K. Regions are numbered and colored the same way as Figure 3. Only hydroxylated regions can be accessed at 873 K, while hydroxyls and triaqua complexes can form at 423 K. Higher surface Co concentration can be reached under low P_{O2}.

Although many possible terminations of this surface exist in theory, not all terminations can be accessed under realistic pressure and temperature. At 423 K (Figure 4, top), only a fraction of the hydroxylated regions (structures 5b, 8b, 9a, 9b, 11a, and 11b) can be visited at equilibrium; though, clear separations among isolated OH, triaqua complexes, and hydroxyl networks can still be observed when P_{H2O} is increased. When O_2 pressure is between 1 bar and 10^{-4} bar, and H_2O pressure is above 10^{-7} bar, the surface is predicted to be heavily hydroxylated, with a triaqua complex incorporated into the OH/H_2O chain (9b). Triaqua complexes is predicted to be separated from the chain below 10^{-7} bar (8b, 9a), and only isolated hydroxyls (5b) are stable below 10^{-12} bar, a moisture level almost impossible to obtain. Overall, at 423 K, the surface stability diagram is dominated by triaqua complex regions with various amounts of additional H_2O/OH groups. On the other hand, if the temperature is increased to 873 K (Figure 4, bottom), isolated hydroxyls will be exposed under 10^{-3} bar. We note that, for the surface Co concentration to increase to above 3.56 Co/nm^2, P_{O2} needs to be reduced to below 10^{-11} bar while P_{H2O} is kept below 10^{-9} bar, i.e. in UHV conditions.

Finally, for reductive reactions involving H_2, we consider the surface to be in equilibrium with H_2 and H_2O. Under these conditions, the system temperature must be kept low, so that kinetics for bulk reduction is slow enough, and the near-surface region is kinetically trapped to retain structure like bulk Co_3O_4. By monitoring the surface oxidation state of NM_1/Co_3O_4 catalysts under NO/H_2 environments via ambient pressure (AP) XPS, Nguyen et al. observed that the near-surface regions generally do not fully reduce to CoO until above 500~600 K.[4] Under H_2/H_2O pressure, the surface stability diagram is as follows:
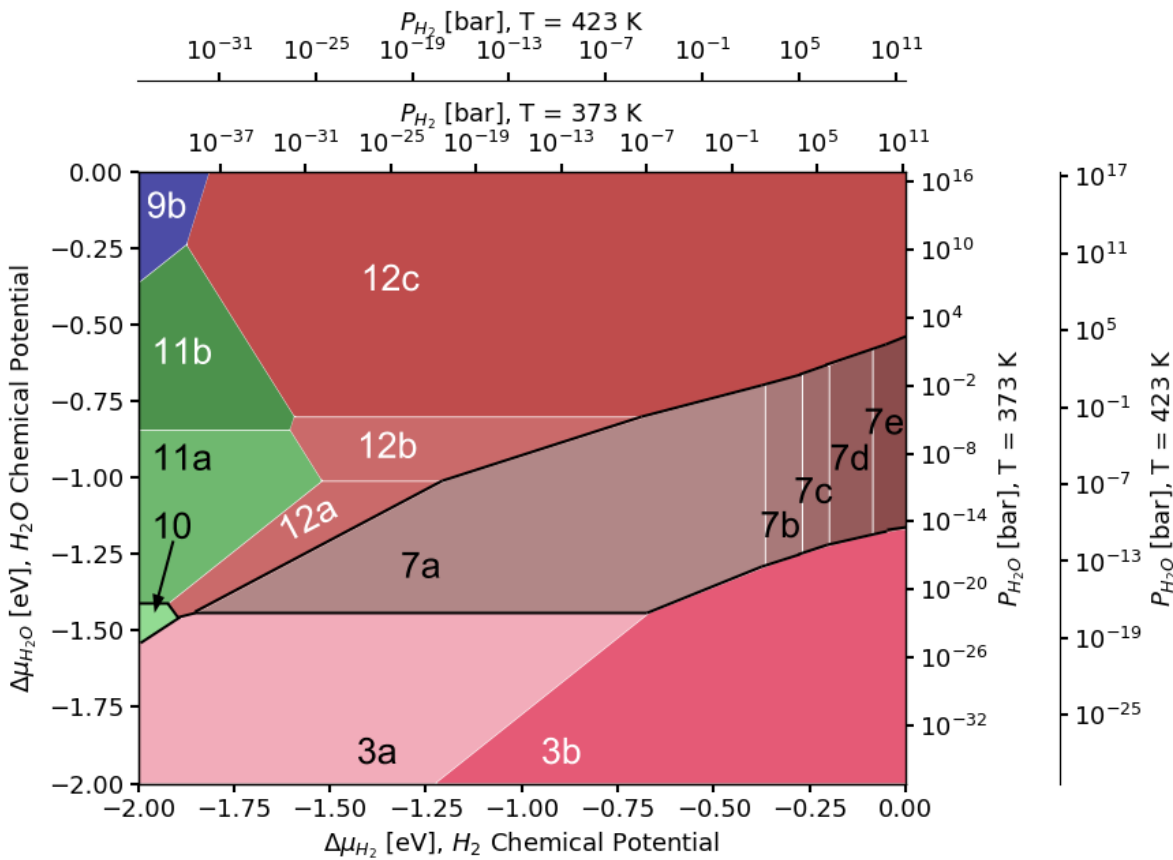
Figure 5. Surface stability diagram showing the most stable surface structure as a function of H_2 and H_2O chemical potential and H_2/H_2O pressure at 423 K. The color scheme and numbering are the same as that in Figure 3. Regions are again classified in same 3 ways as those in Figure 3. I) By surface Co concentration: blue: 3.56 Co/nm^2; green: 5.33 Co/nm^2, and red/brown: 7.11 Co/nm^2. II) By general appearance of surface hydroxylation: bottom bold line separates non-hydroxylated regions and hydroxylated regions and top bold line separates OH-only regions and molecular H_2O-containing structures. III) By specific numbered structure (see Table 1 for descriptions, Table 2 for representative geometries, and Table S11 for all geometries).

Under H_2 and H_2O pressure, separation of non-hydroxylated, hydroxylated, and hydrated regions under H_2/H_2O is also very apparent. When the H_2O chemical potential increases above -1.5 eV, the surface transitions from a vacancy-covered state (representative structure: region 3a, see Table 2, row 1) to a hydroxylated state (representative structure: region 7a, see Table 2, row 5). When H_2O chemical potential increases to above roughly -0.75 ~ -1.00 eV, the surface transitions to a fully hydrated state (representative structure: region 12c, see Table 2, row 10). We note that the bare $(Co^{Oh}Co^{Td})_x$ termination does not appear on the stability diagram. Upon

reduction by H adsorption or O_{vac} formation, the surface undergoes a large relaxation (Figure S13). This relaxation makes vacancy formation much easier than on $(Co^{Oh}Co^{Td})_x$ (Table S6), and H adsorption strong as well (Table S3), but not as strong as that on $(Co^{Td})_x$, which is expected, as the $(Co^{Td})_x$ termination appears overly oxidized. If we again only consider realistic H_2 and H_2O pressures, the surface is dominated by this heavily relaxed hydroxylated region (region 7a in Figure 5, see also Table 2 for structure).
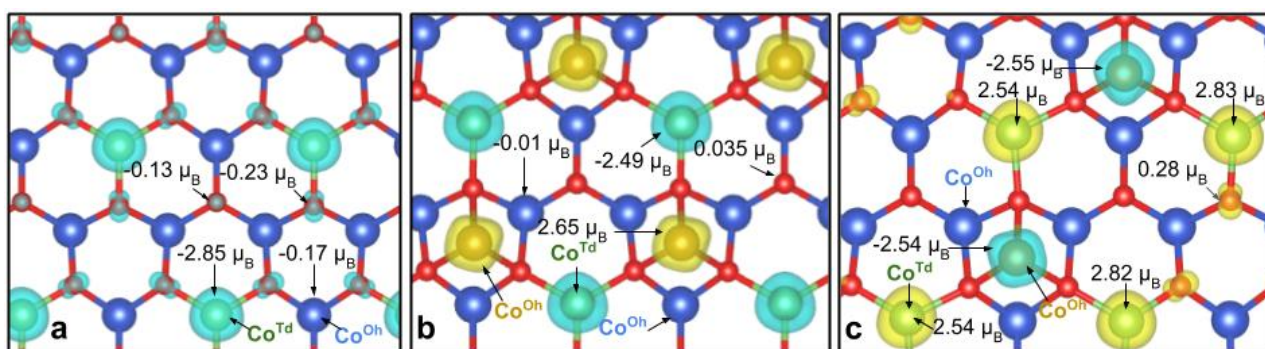
Figure 6. Top view of spin density difference on a) bare $(Co^{Td})_x$, b) bare $(Co^{Oh}Co^{Td})_x$, and c) $(Co^{Oh}_{0.5}Co^{Td})_x$, at isosurface level 0.04, where pale blue represents negative and yellow represents positive spin density difference. Key: Co^{Td}: green, surface Co^{Oh}: gold, subsurface Co^{Oh}: blue. Surface Co (green) on the $(Co^{Td})_x$ termination appear to be slightly more oxidized than bulk Co^{2+}, with slightly higher projected magnetic moments. Charge for this off-stoichiometry is compensated by small density differences on surface O. No projected magnetic moments are found on surface O in the $(Co^{Oh}Co^{Td})_x$ termination. All the added Co appear to be Co^{2+} based on projected magnetic moments, while Co originally on the surface appear slightly reduced. Less Co can be added to the surface to form $(Co^{Oh}_{0.5}Co^{Td})_x$; these Co also appear to be slightly reduced Co^{2+} and quenches spin differences on some surface O.
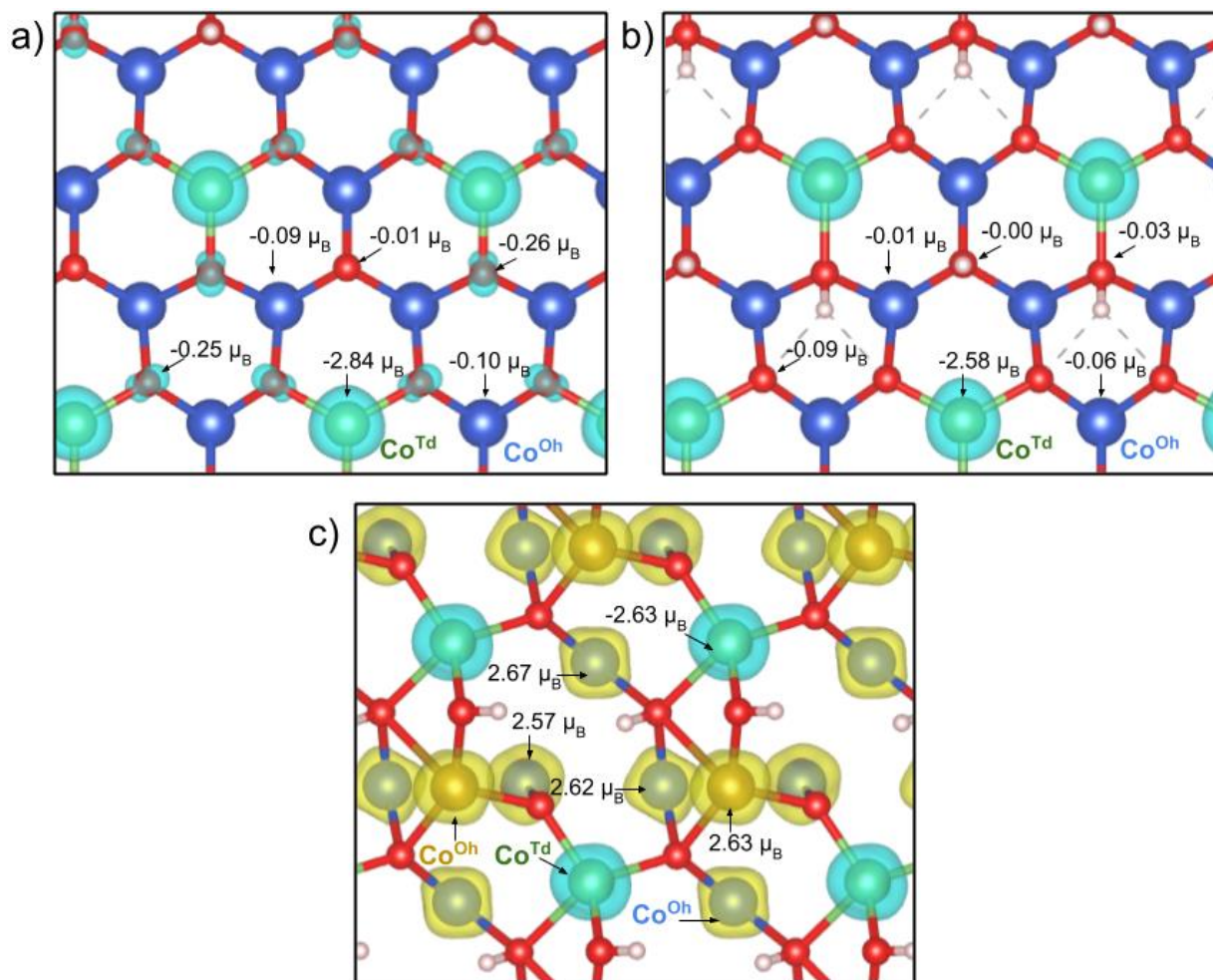
Figure 7. Top view of spin density difference on a) $(Co^{Td})_x$ with 1.78 OH/nm^2, b) $(Co^{Td})_x$ with 7.11 OH/nm^2, and c) $(Co^{Oh}Co^{Td})_x$ with 7.11 OH/nm^2. Key: Co^{Td}: green, surface Co^{Oh}: gold, subsurface Co^{Oh}: blue, H: white. Electrons from adsorbing H on $(Co^{Td})_x$ are transferred to surface O (red), subsurface Co^{Oh}, and surface Co^{Td}. On the other hand, electrons from H adsorption on $(Co^{Oh}Co^{Td})_x$ are transferred mostly to subsurface Co^{Oh}.

Besides surface relaxation, adsorbate-induced charge transfer is very different on the bare Co-rich $(Co^{Oh}Co^{Td})_x$ as well, relative to Co-poor $(Co^{Td})_x$. On $(Co^{Td})_x$, initial H_2 adsorption results in delocalization of charge onto surface O and subsurface Co^{Oh}; the small projected magnetic moments on surface O disappear (Figure 6a, 7a), while subsurface Co's projected magnetic moments decrease in absolute value (from -0.177 μ_B to -0.088 μ_B, Figure 6a, 7a). At a higher OH concentration on $(Co^{Td})_x$, charge is added to surface Co^T, surface O, and subsurface Co^{Oh} as well

20

(Figure 6a, 7b). On the other hand, on the $(Co^{Oh}Co^{Td})_x$ surface, the charge is almost entirely transferred to subsurface Co^{Oh} (Figure 6b, 7c). This result can be rationalized by again considering the overall surface stoichiometry; due to the overoxidized state of the $(Co^{Td})_x$ termination, H_2 adsorbs strongly to balance the stoichiometry. Further, the $(Co^{Oh}Co^{Td})_x$ slab is closer to that of CoO, whereas the $(Co^{Td})_x$ is closer to Co_2O_3, making near-surface Co atoms in the $(Co^{Td})_x$ slab closer to Co^{3+}, and near-surface Co in $(Co^{Oh}Co^{Td})_x$ closer to Co^{2+}. By the spectrochemical series, Co^{2+} induces a much smaller crystal field splitting than Co^{3+}, and as a result, subsurface Co on reduced $(Co^{Td})_x$ have magnetic moment smaller than 1 μ_B, while those on $(Co^{Oh}Co^{Td})_x$ have magnetic moment closer to 2.6 μ_B (Figure 7b, 7c).

3.2   Comparison to experimental results reached through vibrational spectroscopy

Experimental characterization of surface hydroxyls on Co_3O_4 by vibrational spectroscopy is difficult, but not impossible. In Busca et al.'s *ex situ* IR investigation of air-calcined, then reduced Co_3O_4, the v(OH) IR window was open when the surface is reduced in 200 Torr of H_2 at 523 K.[16] Upon evacuation at 373 K, v(OH) on the reduced Co_3O_4 were observed at 3680, 3658, 3630, and ~3580 cm^{-1}, with an additional broad band centered at 3330 cm^{-1}.[16] Assuming the particle did not reshape during the H_2 treatment, some OH modes remaining after evacuation should correspond to those observed on the equilibrated reduced (111) surface.

Vibrational spectroscopy after treatment only by water has also been performed by various groups on this surface. Petitto et al. performed *ex situ* HREELS on a single (111) terminated Co_3O_4 crystal after annealing at 623 K under 6.6 x 10^{-5} Pa H_2O, cooling down to 110 K, and flashing to 400 K to remove molecular water, all in the absence of H_2 reduction.[21] They observed a single v(OH) peak located at 3650 cm^{-1}.[21] Through *in situ* IRAS at 500 K under 3.0 × 10^{-7} mbar D_2O, Schwarz et al. reached a similar result on Co^{2+} and O^{2-} terminated Co_3O_4(111)

21

thin films.[22] They found a single $v(OD)$ peak at 2650 cm^{-1}. They also observed the surface's hydroxylation behavior changing drastically in the interval of 200 K – 500 K under the same pressure. Two broad hydroxyl peaks appear at 2715 cm^{-1} and 2550 cm^{-1} at 200 K, while an array of sharp, discrete peaks of variable intensity appear in the range 2730 cm^{-1} to 2500 cm^{-1} between 300 K and 400 K.

Table 3. Gas phase conditions reached in vibrational spectroscopy above 500 K

Reference	*Conditions: T [K] and P_i [bar]*	*Conditions: $\Delta\mu_i$ [eV]*
Busca et al.[16]	T = 523 K, P_{H2} = 0.27 bar	$\Delta\mu_{H2}$ = -0.70 eV
Petitto et al.[21]	T = 623 K, P_{H2O} = 6.6 x 10^{-10} bar P_{O2} = 4 x 10^{-10} ~ 4 x 10^{-16} bar	$\Delta\mu_{H2O}$ = -2.30 eV $\Delta\mu_{O}$ = -1.22 ~ -1.60 eV
Schwarz et al. [22,23]	T = 200 K, P_{D2O} = 3 x 10^{-11} bar P_{O2} = 10^{-10} ~ 10^{-16} bar T = 300 K, P_{D2O} = 3 x 10^{-11} bar P_{O2} = 10^{-10} ~ 10^{-16} bar T = 370 K, P_{D2O} = 3 x 10^{-11} bar P_{O2} = 10^{-10} ~ 10^{-16} bar T = 500 K, P_{D2O} = 3 x 10^{-11} bar P_{O2} = 10^{-10} ~ 10^{-16} bar	$\Delta\mu_{D2O}$ = -0.74 eV $\Delta\mu_{O}$ = -0.37 ~ -0.49 eV $\Delta\mu_{D2O}$ = -1.14 eV $\Delta\mu_{O}$ = -0.57 ~ -0.75 eV $\Delta\mu_{D2O}$ = -1.43 eV $\Delta\mu_{O}$ = -0.71 ~ -0.93 eV $\Delta\mu_{D2O}$ = -1.98 eV $\Delta\mu_{O}$ = -0.99 ~ -1.29 eV
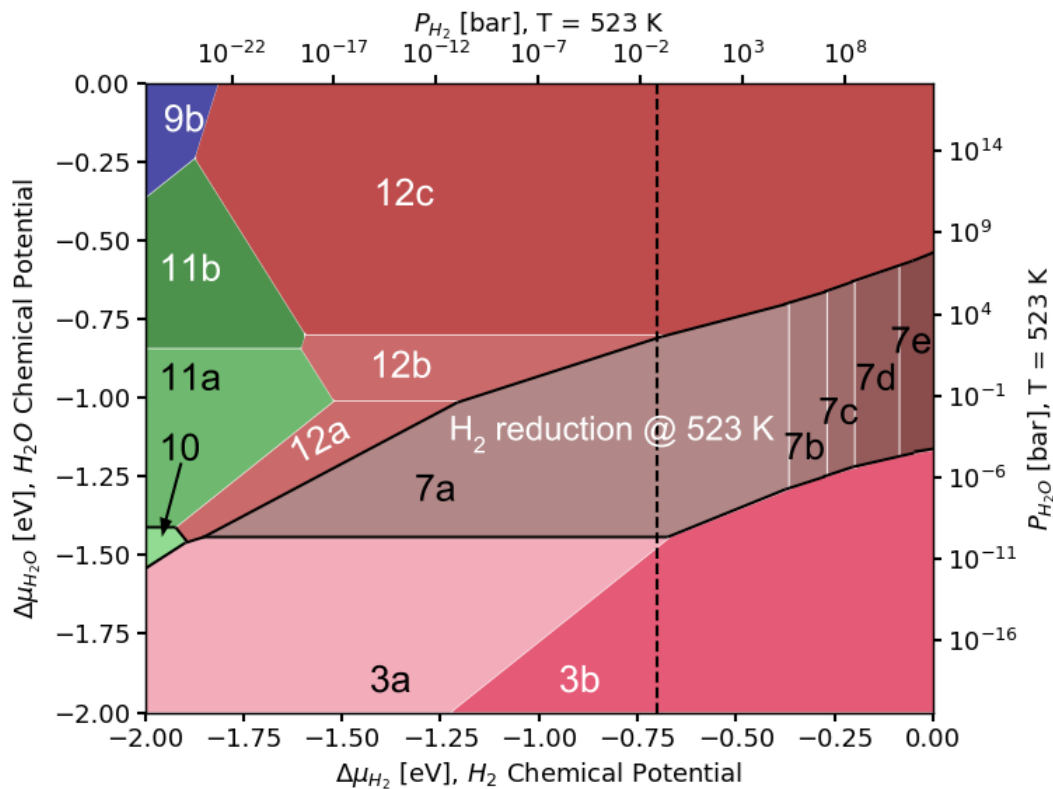
Figure 8. Gas phase environmental conditions during vibrational characterization by Busca et al. represented as a dashed line on the H_2O/H_2 surface stability diagram (Figure 5), as H_2O chemical potential is not well-defined. The corresponding termination should contain 7.11 Co/nm^2 and 7.11 OH/nm^2 (structure 7a, brown) because an unrealistic high pressure of H_2O must be applied to generate a mixed OH/H_2O layer (structure 12c, red).
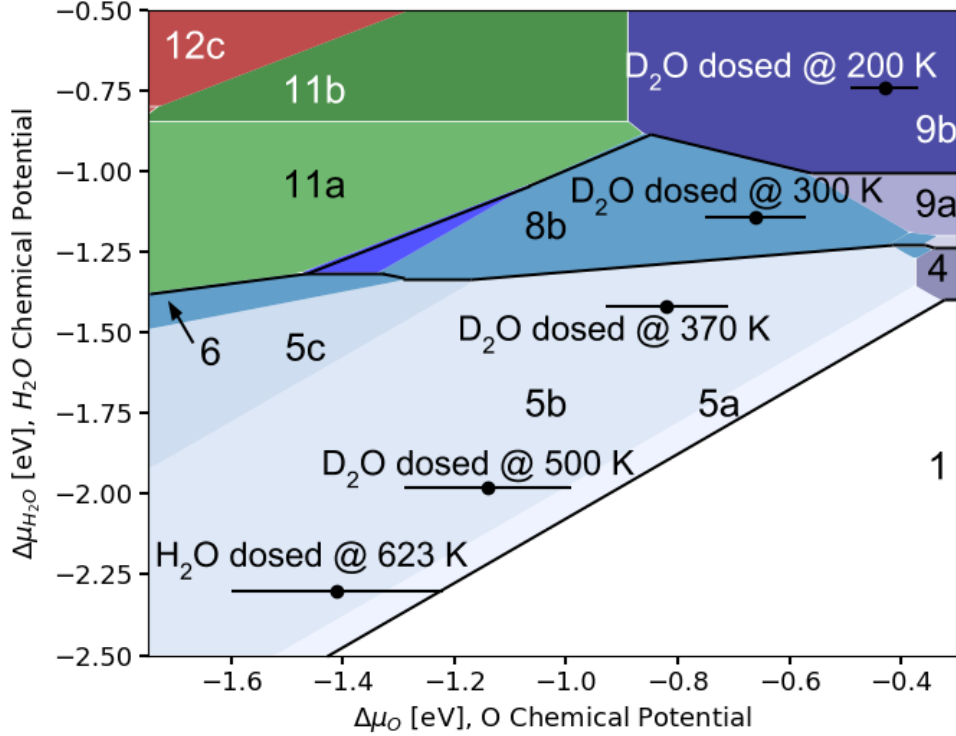
Figure 9. Gas phase environmental conditions during vibrational characterization under H_2O/D_2O pressure, overlaid with the H_2O/O surface stability diagram of Figure 3. These conditions fall under three main regions: $(Co^T)_x$ with triaqua-complex-incorporated OH/H_2O chains (structure 9b), triaqua surface complex with additional OH (8b) for D_2O dosed at 200 K and 300 K, and $(Co^T)_x$ with isolated OH (structure 5b) for D_2O exposure at 370 K and beyond. Gas phase conditions in characterization experiments are marked as dots with error bars for O chemical potential.

In our previous work, we identified three main structures observed on $(Co^{Td})_x$ surface upon exposure to 3 x 10^{-8} mbar D_2O at 300 K, without considering any surface reduction. The three motifs are: i) isolated hydroxyls, ii) surface $Co(H_2O)_3$ complexes, and iii) extended hydroxyl networks.[49] Here, accounting for the effect of O_2 in the atmosphere, we provide an O_2-equilibrated view of the hydroxylation behavior observed on $Co_3O_4(111)$ films during and after the experiments described. Through interpolation of experimental thermochemistry data, the conditions produced by the H_2, H_2O, and D_2O treatments can be converted to a set of water and hydrogen or oxygen chemical potentials (Table 3) and overlaid on the stability diagrams (Figure 8, 9). Since no *in situ* spectra are available under the conditions of Busca et al.'s and Petitto et

al.'s experiments, we assume that cooling and evacuation does not disrupt the surface structures generated during H_2 and H_2O treatments. To approximate the oxygen content in the atmosphere observed in the water exposure experiments, we consider three magnitudes above and below the vacuum level in the experiments to calculate a possible range of chemical potentials for the conditions. For the H_2-exposure experiment, we consider the range of water pressures that can be realistically reached to set a possible range of water chemical potentials.

In *ex situ* IR after H_2 reduction and evacuation, multiple types of hydroxyl groups remain on the surface.[16] This result can be attributed to the large variation of exposed surfaces on a Co_3O_4 particle.[10] Our calculations show that for the (111) surface, the $(Co^{Oh}Co^{Td})_x$ termination (7.11 Co/nm^2) with 7.11 OH/nm^2 (structure 7a) is most likely exposed (Figure 8).[16] Two types of OH groups can be found on this surface: a bidentate OH group and a tetradentate OH group (see Table 2), which we found to exhibit 3667~3668 cm^{-1} and 3527~3528 cm^{-1} ν(OH) modes respectively. These modes are close to two reported values (3680 cm^{-1} and 3580 cm^{-1}) out of many modes found by Busca et al. It is suggested that other modes are associated with other terminations of Co_3O_4. We did not consider the hydroxyl overlayer structure (structure 12c) in our assessment because P_{H2O} must be unrealistically high at 523 K for the fully hydroxylated structure to exist.

Since no H_2 is present in the gas phase in the preparation of $Co_3O_4(111)$ films and D_2O/H_2O exposure experiments of Schwarz et al., we considered the surfaces to be in equilibrium with an oxygen pressure 3 magnitudes about the vacuum level. With P_{O2} in consideration, we predict the following structures. D_2O exposure at 200 K, compared to our previous investigation, still corresponds to a hydrogen bonded hydroxyl network containing a triaqua complex (structure 9b). Next, D_2O exposure at 300 K corresponds to triaqua complexes

immediately surrounded by OD (structure 8b). The $Co(D_2O)_3$+OD structure shows modes in the range 2715~2723 cm^{-1}, belonging to the v(OD) modes of the triaqua surface complex, and modes in the range 2547~2551 cm^{-1} belonging to OD surrounding the complex. This result shows that the triaqua surface complex is robust and insensitive to surrounding OH. Finally, the conditions obtained by H_2O or D_2O adsorption experiments 370 K and above by Petitto et al. and Schwarz et al. fall under the sparsely hydroxylated region (structure 5b). Surface tridentate modes are located at 2684 cm^{-1}/2681 cm^{-1} for OD and 3637 cm^{-1}/3633 cm^{-1} for OH. These results match those obtained by Petitto et al. after purging physisorbed water (3645 cm^{-1}) and the OD bands are 25-35 cm^{-1} away from D_2O adsorption modes found by Schwarz et al. (2657 cm^{-1}).

Previously, through a comparison between $D_2{}^{18}O$ and $D_2{}^{16}O$ exposure IRAS, it was shown that O of isolated surface OD generated through D_2O exposure above 500 K originate from the surface, since the v(OD) modes are not modified upon change of O isotope in water. Here, since we assume that no H_2 is present in the atmosphere, the only way to generate only these hydroxyls is through vacancy re-filling by D_2O, and diffusion of the proton to surface O atoms. Upon $D_2{}^{18}O$ dissociation at vacancy, one ^{18}OD and one ^{16}OD are generated, but since the surface is still rich in ^{16}O, v(^{16}OD) will be the predominant peaks in the IR spectrum. Another hypothesis is that eventual OD groups from water have low intensity in the spectrum.[49]

3.3   Comparison among U_{eff} = 3.5 eV, 2.0 eV, and HSE06

The DFT+U approach is a very popular method used to describe strongly correlated systems as it makes a good compromise between accuracy and feasibility. The most popular adaptation is the rotationally-invariant method of Dudarev et al., where only one quadratic on-

site self-interaction penalty is added to the DFT energy to enforce integer occupancies in each spin orbital of the orbitals of interest.[37] Choosing an appropriate U_{eff} value to use is a very controversial topic in DFT modeling of strongly correlated systems.[50]

Approaches taken in literature can be divided to two categories: directly computing U_{eff} through linear response to correct DFT's unphysical energy response to addition and removal of fractional numbers of electrons and 2) fitting some empirical properties of the system. Studies using both approaches have been performed for the Co_3O_4 bulk and surfaces. Chen et al. calculated U_{eff} of Co^{2+} and Co^{3+} in bulk Co_3O_4 and used the weighted average, 5.9 eV, to study bulk properties; however, the approach predicted the ferromagnetic ground state being more favorable.[9] The approach also does not predict well surface and bulk redox properties.[26,51] The U_{eff} determined through this approach is also unique to the calculation method; a later study performed using PAW pseudopotentials in VASP, instead of Troullier-Martins pseudopotentials in Quantum Espresso found U_{eff} of Co^{2+} and Co^{3+} at bulk sites to be 4.3 eV and 5.02 eV.[25]

Since the Co linear response U_{eff} does not predict well redox properties, authors interested in reactive properties tend to choose smaller values. Bajdich et al. and Chen et al. have noted that $U_{eff} \sim 3$ eV is optimal to properly describe reactivity.[51,52] Jiang et al. used $U_{eff} = 2.0$ eV to match bulk band gap with experiment.[29] Recently, Hu et al., using results obtained from RPA as benchmarks, proposed the usage of two different values of U_{eff}, applied to the Co and surface Co atoms respectively, to examine the reactivity of oxygen-rich $Co_3O_4(110)$.[53] To ensure that our choice of $U_{eff} = 3.5$ eV is appropriate for $Co_3O_4(111)$, we compared energies of water adsorption and O vacancy formation generated at this U_{eff} to those obtained using $U_{eff} = 2.0$ eV and HSE06+dDsC. We chose the value of $U_{eff} = 2.0$ eV in addition to our initial choice $U_{eff} = 3.5$ eV, as it is a very popular value used in many DFT studies on the reactivity of Co_3O_4 surfaces. Table

4 compares energy of vacancy formation, for $O_{vac} = 3.56$ nm^{-2} and energy of adsorption of water at 3.56 H$_2$O/nm^2 and 7.11 OH/nm^2, reached using the three methods on the $(Co^{Td})_x$ termination of Co$_3$O$_4$.

Table 4. Comparison of water adsorption energy and energy of vacancy formation calculated using U_{eff} = 3.5 eV, 2.0 eV, and HSE06+dDsC (water adsorption data adapted from [49])

Description	Energy [eV], U_{eff}=3.5 eV	Energy [eV], U_{eff}=2.0 eV	Energy [eV], HSE06+dDsC
Vacancy formation, $(Co^T)_x$ with 3.56 O_{vac}/nm^2, energy of O_{vac} formation, E_{form} per O_{vac}	2.07	3.01	2.31
Water adsorption, $(Co^T)_x$ with 7.11 OH/nm^2 and 3.56 H$_2$O/nm^2 in the "pair" configuration (see SI, Figure S13, top), E_{ads} per H$_2$O molecule	-1.02	-0.91	-1.08
Water adsorption, $(Co^T)_x$ with 7.11 OH/nm^2 and 3.56 H$_2$O/nm^2 in the "hexagonal" configuration (see SI, Figure S13, bottom), E_{ads} per H$_2$O molecule	-1.00	-0.96	-1.10

As seen in the table above, the energy of vacancy formation decreases as U_{eff} increases. Upon generation of a single O_{vac} on this termination, electrons are transferred to the Co atoms immediately surrounding the vacancy. Increasing U_{eff} increases the penalty placed on delocalization while facilitating electron localization. Selcuk and Selloni also observed that O vacancy formation energy on the (110) surface, in the case where electrons are localized, heavily depends on U_{eff}.[26] On the other hand, the adsorption of water is an electron-neutral process, which explains why the change in E_{ads} is not very significant. These adsorption results obtained from U_{eff} = 3.5 eV do not strongly differ from those at U_{eff} = 2 eV but agree better with results from HSE06.

For further confirmation, we recalculated using U_{eff} = 2.0 eV the surface energy of structures shown in Figure 9 and Table 4 and constructed an analogous surface stability diagram combined shown on Figure 10.
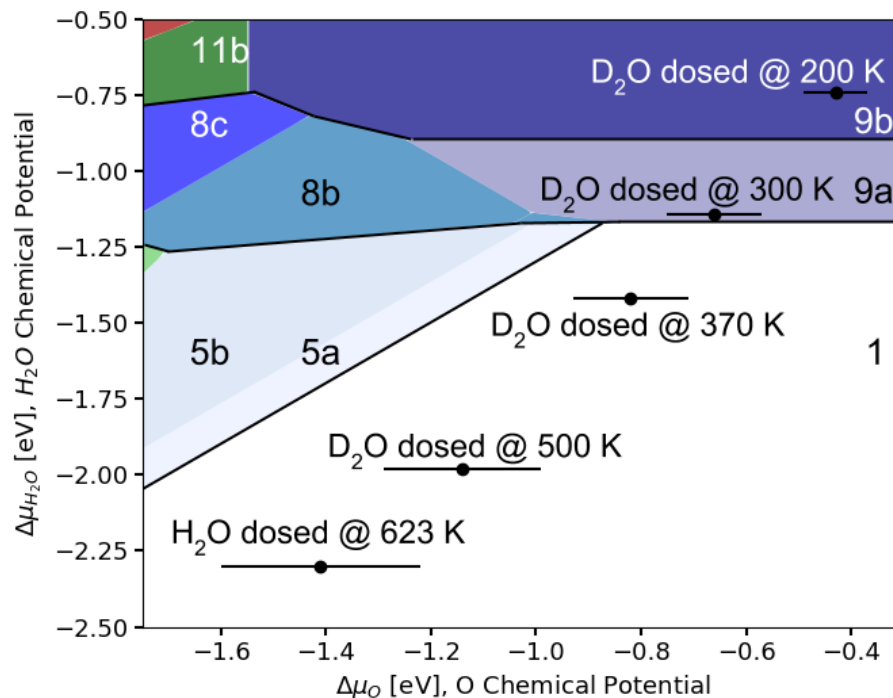
Figure 10. Surface structure as a function of oxygen and water chemical potential calculated using U_{eff} = 2.0 eV. Gas phase conditions observed in vibrational characterization are marked as dots with error bars for O chemical potential. No hydroxylation is predicted to exist in D_2O/H_2O exposure conditions at 370 K and above when using U_{eff} = 2.0 eV.

The lower U_{eff} value heavily decreases the energy of adsorption of hydrogen and weakens slightly water adsorption. Interestingly, the stability diagram reached from U_{eff} = 2.0 eV does not predict hydroxylation through D_2O exposure or annealing in H_2O, in contrast with experiments. The value U_{eff} = 3.5 eV hence produces results that match much better the spectroscopic experiments. Like vacancy formation, H adsorption adds electrons to the surface and becomes expectedly more favorable with increasing U_{eff}. Altogether, these test results validate the theoretical method used in the present paper.

3.4   Predicted surface structure under catalytic reaction conditions

Co_3O_3's applications in thermal catalysis can be divided into three categories. First, Co_3O_4 has been known as an effective CO and hydrocarbon oxidation catalyst.[1,54–56] Xie et al. found that CO oxidation can occur over Co_3O_4 nanorods at a temperature as low as -77 ℃, but is easily poisoned by water.[54,55] The activity appears to depend on the exposed surfaces and catalyst shape.[57] Second, Co_3O_4 can also be used as a catalyst or support for NO_x reduction.[1,3,4,58,59] N_2O decomposition to N_2 and O_2 over Co_3O_4 was found to occur at 873 K, and selective catalytic reduction (SCR) reaction of NO with NH_3 and O_2 was found to occur over Co_3O_4 at 423 K.[3,58] NO reduction with H_2 can also be performed over single noble metal (NM) atoms anchored on Co_3O_4 to produce N_2 or N_2O.[4,60] Third, one promising application of the (111) surface is the oxidative dehydrogenation (ODH) of alkanes.[5–7] This reaction was explored by Tyo et al., Liu et al, and Fung et al.[5–7] It was found that the alkane activation occurs over one isolated surface O and one O adjacent to surface Co (see Section 2.2), and that substitution of surface Co-T_d with other metals lowers the activation barrier of alkanes by increasing surface reducibility.[61] Liu et al. showed that Co_3O_4 particles primarily exposing the (111) facet have higher conversion and selectivity for ethane ODH than particles that expose higher miller index surfaces such as (311).[62] Overall, reactions using Co_3O_4 as a catalyst or support and containing O_2 in the atmosphere are performed below 900 K, and reactions using H_2/H_2O as reactant/product are performed below 500-600 K.

30

Table 5. Gas phase conditions observed in catalytic reactions

| Reaction	Conditions: T [K] and P_i [bar]	Conditions: $\Delta\mu_i$ [eV]
$2CO + O_2 \rightarrow 2CO_2$ [54]	T = 196 K, P_{O2} = 0.02 bar	$\Delta\mu_O$ = -0.20 eV
$2N_2O \rightarrow 2N_2 + O_2$ [58]	T = 873 K, P_{O2} = 2 x 10^{-3} bar	$\Delta\mu_O$ = -1.17 eV
$2C_2H_6 + O_2 \rightarrow 2C_2H_4 + 2H_2O$ $2C_2H_6 + 7O_2 \rightarrow 4CO_2 + 6H_2O$ [7]	T = 873 K, P_{O2} = 0.018 bar P_{H2O} = 0.033 bar	$\Delta\mu_O$ = -1.09 eV $\Delta\mu_{H2O}$ = -2.00 eV
$CH_4 + 2O_2 \rightarrow CO_2 + 2H_2O$ $2CH_4 + 3O_2 \rightarrow 2CO + 4H_2O$ [63]	T = 873 K, P_{O2} = 0.0017 bar P_{H2O} = 0.0050 bar	$\Delta\mu_O$ = -1.18 eV $\Delta\mu_{H2O}$ = -2.14 eV
$2NO + 2H_2 \rightarrow N_2 + 2H_2O$ $2NO + H_2 \rightarrow N_2O + H_2O$ [4]	T = 423 K, P_{H2} = 0.0095 bar P_{H2O} = 0.040 bar	$\Delta\mu_{H2}$ = -0.66 eV $\Delta\mu_{H2O}$ = -0.85 eV
	T = 523 K, P_{H2} = 0.00049 bar P_{H2O} = 0.0483 bar	$\Delta\mu_{H2}$ = -0.98 eV $\Delta\mu_{H2O}$ = -1.08 eV
$4NO + 4NH_3 + O_2 \rightarrow 4N_2 + 6H_2O$ [3]	T = 423 K, P_{O2} = 0.020 bar P_{H2O} = 6 x 10^{-4} bar	$\Delta\mu_O$ = -0.48 eV $\Delta\mu_{H2O}$ = -1.00 eV
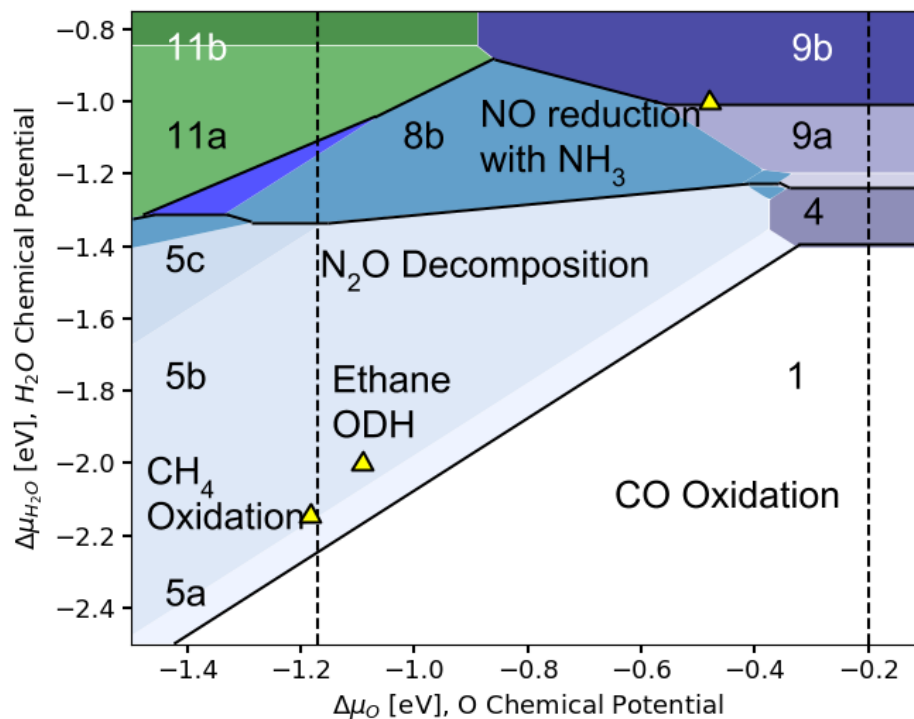
Figure 11. Surface stability diagram as a function of O_2 and H_2O chemical potential. Conditions in low temperature CO oxidation, N_2O decomposition, ethane ODH, CH_4 oxidation, and NO reduction with NH_3 are marked on the diagram as yellow triangles if P_{H2O} is well-defined and dashed lines otherwise.

Reactive conditions considered in this work are listed on Table 5. H_2, O_2, and H_2O are assumed to be ideal gases, and their partial pressures are estimated using the reported reaction conversion and selectivity, assuming the reactions take place isobarically at 1 bar. Co_3O_4 is most commonly used for oxidative reactions without H_2; therefore, in most gas phase reactions, the Co_3O_4 surfaces are in equilibrium with H_2O and O_2. Let us start this discussion with low temperature CO oxidation. Since the water chemical potential is not clearly defined for that reaction, conditions are indicated as a dashed vertical line on the right side of Figure 11. However, the nature of the $Co_3O_4(111)$ surface can change quite drastically when water is present. In these conditions, from our calculations (Figure 11), hydroxyls will populate the surface when water chemical potential is greater than -1.45 eV, which, at 196 K, corresponds roughly to a pressure higher than 10^{-30} bar; in other words, any water present will contaminate the surface. As the reaction temperature increases at the same O_2 pressure, the surface becomes less susceptible to hydroxylation. CO TPD studies have also shown that lattice oxygen does not appear to be reactive; therefore, it is crucial for surface Co^{2+} to be exposed during CO oxidation to adsorb reactants.[64] At 196 K, under the O_2 pressure applied in the CO oxidation reaction, the surface already becomes covered with an triaqua-complex-containing H_2O/OH overlayer (structure 9b) when P_{H2O} is in the order of 10^{-15} bar. Both experimentally determined and calculated energy of CO adsorption falls far above -1.1 eV, indicating that any water impurities will completely block the reaction, in agreement with experiments.[64,65] Conditions for N_2O decomposition also correspond to a line on Figure 11, but at a lower O chemical potential, mainly from the much higher temperature. The surface structure during N_2O decomposition is also dependent on the amount of H_2O impurities in the gas phase; though, the only accessible regions, i.e. $P_{H2O} > 10^{-12}$ bar and above, are the bare $(Co^{Td})_x$ and $(Co^{Td})_x$ terminations with ≤ 1.78

32

OH/nm^2 (5a, 5b). The transition from bare to hydroxylated can occur very easily, but no hydroxyl cluster or overlayer can form.

Reactions that generate H$_2$O, as a product or side product, also carry the threat that the Co$_3$O$_4$ surface will hydroxylate. In the conditions associated to the ODH of ethane, the surface is found to be slightly hydroxylated, with 1.78 OH/nm^2 (structure 5b). CH$_4$ oxidation would also fall under the same region on the phase diagram. Both reactions occur at high temperatures, so it is reasonable to expect the surfaces to have low degrees of hydroxylation. Finally, for NO reduction with NH$_3$, the conditions for this reaction fall at the boundary between the zone of triaqua-complex-containing OH/H$_2$O chains (9b) and triaqua complex/OH/H$_2$O chain existing separately (8b). In other words, surface Co is unlikely to be exposed during this reaction.
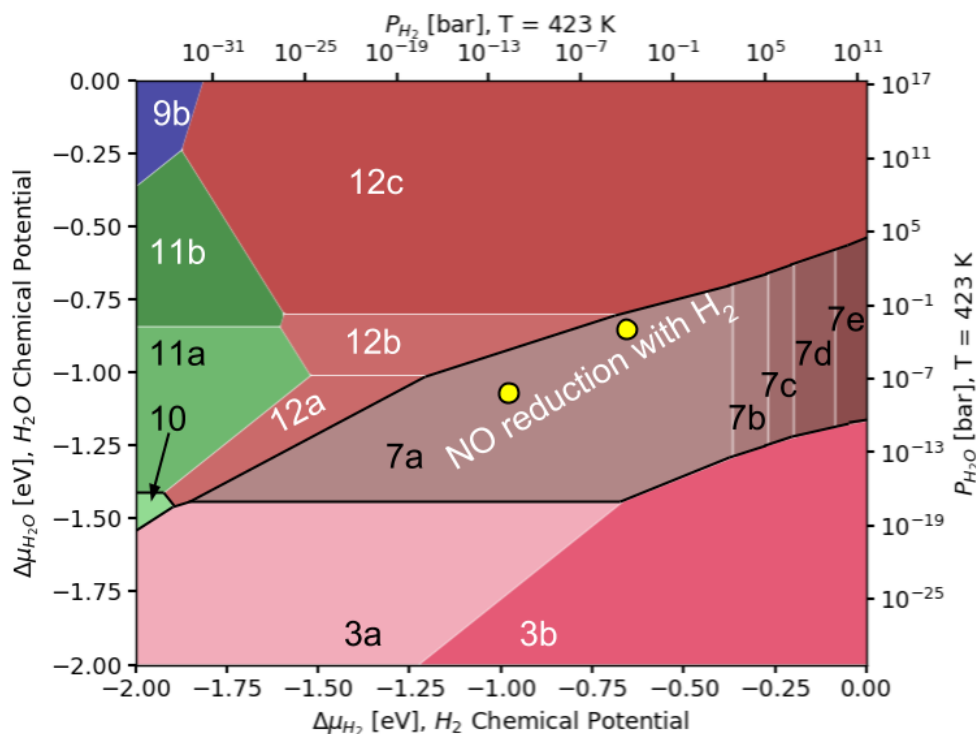

Figure 12. Surface stability diagram as a function of H$_2$ and H$_2$O chemical potential and hydrogen/water pressure at 423 K. Conditions in NO reduction with H$_2$ found in the literature are marked on the diagram as yellow circles.

On the other hand, the environment during NO reduction with H_2 equilibrates the surface with H_2O and H_2 (Figure 12). In this reaction, the Co_3O_4 plays the role of support for noble metal atoms (Pd, Pt, and Rh; the conditions here refer to NO reduction over Pd/Co_3O_4), and it was observed through AP-XPS that when the temperature is moderate enough, surface transition to CoO is inhibited.[4,60] In these conditions, the $(Co^{Oh}Co^{Td})_x$ surface with 7.11 OH/nm^2 (structure 7a) would be exposed. The high coverage of hydroxyl groups present might, however, play a major role in modifying the catalysts support interaction and the nature of the charge transfer between the support and the metallic nanoparticle.[66]

4.   Conclusion

In this study, we investigated the surface structure of three terminations of $Co_3O_4(111)$ in equilibrium with a wide range of gas environments and mapped out detailed surface stability diagrams with respect to vacancy formation and hydroxylation of the surface either from hydrogen or water adsorption. We found that all three terminations are accessible, but the Co-poor ($(Co^{Td})_x$, 3.56 Co/nm^2) and Co-rich ($(Co^{Oh}Co^{Td})_x$, 7.11 Co/nm^2) terminations are the most prevalent. When equilibrated with oxygen and water, we found that the Co-poor termination exhibits three stages of hydroxylation – formation of isolated OH at low $\Delta\mu_{H2O}$, transition to isolated OH/H_2O clusters when $\Delta\mu_{H2O} > -1.3$ eV, and finally to a fully hydrated state when $\Delta\mu_{H2O} > -1.0$ eV.

We found that if the surface is in equilibrium with oxygen, the Co-poor/O-rich surface $(Co^{Td})_x$ is predominantly exposed, and it is very difficult to produce the stoichiometric $(Co^{Oh}_{0.5}Co^{Td})_x$ or the Co-enriched $(Co^{Oh}Co^{Td})_x$ termination. Since we found it to be very easy to populate the $(Co^{Td})_x$ surface with hydroxyls through H_2 adsorption or H_2O dissociation over a

vacancy, we predict that hydroxyls will appear during oxidative reactions that produce water or even when water is present as an impurity at low partial pressure. We compared the calculations results concerning hydroxylation of $(Co^{Td})_x$ to those obtained from vibrational spectroscopy on Co_3O_4 single crystals and $Co_3O_4(111)$ films and conclude that at low and medium temperature triaqua surface complexes surrounded by OH/H_2O groups are observed, while only isolated OH are present at higher temperature. In a similar way, unless the environment contains very little water, the O-poor termination $(Co^{Oh}Co^{Td})_x$ is predicted also be hydroxylated.

We found that stabilization of the stoichiometric termination $(Co^{Oh}_{0.5}Co^{Td})_x$ and Co-rich termination $(Co^{Oh}Co^{Td})_x$ is only possible under vacuum at high temperature and in hydrogen and water at low temperatures. The H_2/H_2O conditions are the most important for catalytic applications. We found that reduction of this Co-rich termination through H adsorption and O_{vac} formation is easy due to the large relaxation observed at 7.11 OH/nm^2 or 3.56 O_{vac}/nm^2. At 423 K and below and under realistic H_2/H_2O pressure, the $(Co^{Oh}Co^{Td})_x$ termination with 7.11 OH/nm^2 is highly stable. The OH groups on that termination exhibit vibrational frequencies that fall under the range observed in *ex situ* IR experiments. We believe that this termination should be considered when modeling reactions over Co_3O_4 in low temperature reducing environments.

We validated our results through changing the U_{eff} value and comparing with results reached through hybrid functionals. We found good agreement with both macroscopic experimental observations and HSE06+dDsC calculations using $U_{eff} = 3.5$ eV. Hence, the various terminations of Co_3O_4 should be hydroxylated under a large range of conditions. It is therefore of high importance to include a correct coverage in hydroxyl groups for a realistic modelling of the Co_3O_4 surface in calculations; the bare surface model usually used in reaction pathway calculations might not be adequate. The effect of hydroxyls in the modification of

reaction mechanisms and their interactions with supported metal atoms/clusters must also be considered. Further studies will focus on the interaction among various surface features discussed in this work, and the implications of these structures on the surface's reactivity and properties of the supported active sites.

5. Acknowledgements

6. Supplementary materials:

1) Surface energy calculation details, 1-dimensional surface stability diagrams, energies of adsorption, energies of vacancy formation, top/side views of geometries, and other details available in supporting information (1)

2) Geometries of all structures referenced in this work are available in supporting information (2)

7. References

(1)   Sun, H.; Ang, H. M.; Tade, M. O.; Wang, S. Co3O4 Nanocrystals with Predominantly Exposed Facets: Synthesis, Environmental and Energy Applications. *J. Mater. Chem. A* **2013**, *1*, 14427–14442.

(2)   Zhang, S.; Shan, J.; Zhu, Y.; Frenkel, A. I.; Patlolla, A.; Huang, W.; Yoon, S. J.; Wang, L.; Yoshida, H.; Takeda, S.; Tao, F. (Feng). WGS Catalysis and In Situ Studies of CoO(1–x) , PtCo(n)/Co3O4 , and Pt(m)Co(m)/CoO(1–x) Nanorod Catalysts. *J. Am. Chem. Soc.* **2013**, *135*, 8283–8293.

(3)   Meng, B.; Zhao, Z.; Wang, X.; Liang, J.; Qiu, J. Selective Catalytic Reduction of Nitrogen Oxides by Ammonia over Co3O4nanocrystals with Different Shapes. *Appl. Catal. B Environ.* **2013**, *129*, 491–500.

(4)   Nguyen, L.; Zhang, S.; Wang, L.; Li, Y.; Yoshida, H.; Patlolla, A.; Takeda, S.; Frenkel, A. I.; Tao, F. Reduction of Nitric Oxide with Hydrogen on Catalysts of Singly Dispersed Bimetallic Sites Pt1Co(m) and Pd1Co(N). *ACS Catal.* **2016**, *6*, 840–850.

(5)   Tyo, E. C.; Yin, C.; Di Vece, M.; Qian, Q.; Kwon, G.; Lee, S.; Lee, B.; Debartolo, J. E.; Seifert, S.; Winans, R. E.; Si, R.; Ricks, B.; Goergen, S.; Rutter, M.; Zugic, B.; Flytzani-Stephanopoulos, M.; Wang, Z. W.; Palmer, R. E.; Neurock, M.; Vajda, S. Oxidative Dehydrogenation of Cyclohexane on Cobalt Oxide (Co3O4) Nanoparticles: The Effect of Particle Size on Activity and Selectivity. *ACS Catal.* **2012**, *2*, 2409–2423.

(6)   Fung, V.; Tao, F. (Feng); Jiang, D. Understanding Oxidative Dehydrogenation of Ethane on Co $_3$ O $_4$ Nanorods from Density Functional Theory. *Catal. Sci. Technol.* **2016**, *6*, 6861–6869.

(7)   Liu, J.; Fung, V.; Wang, Y.; Du, K.; Zhang, S.; Nguyen, L.; Tang, Y.; Fan, J.; Jiang, D.; Tao, F. F. Promotion of Catalytic Selectivity on Transition Metal Oxide through Restructuring Surface Lattice. *Appl. Catal. B Environ.* **2018**, *237*, 957–969.

(8)   Roth, W. L. The Magnetic Structure of Co3O4. *J. Phys. Chem. Solids* **1964**, *25*, 1–10.

(9)   Chen, J.; Wu, X.; Selloni, A. Electronic Structure and Bonding Properties of Cobalt Oxide in the Spinel Structure. *Phys. Rev. B* **2011**, *83*, 245204.

(10)   Zasada, F.; Piskorz, W.; Stelmachowski, P.; Kotarba, A.; Paul, J. F.; Płociński, T.; Kurzydłowski, K. J.; Sojka, Z. Periodic DFT and HR-STEM Studies of Surface Structure and Morphology of Cobalt Spinel Nanocrystals. Retrieving 3D Shapes from 2D Images. *J. Phys. Chem. C* **2011**, *115*, 6423–6432.

(11)   Meyer, W.; Biedermann, K.; Gubo, M.; Hammer, L.; Heinz, K. Surface Structure of Polar Co3O4(111) Films Grown Epitaxially on Ir(100)-(1 × 1). *J. Phys. Condens. Matter* **2008**, *20*.

(12)   Goniakowski, J.; Finocchi, F.; Noguera, C. Polarity of Oxide Surfaces and Nanostructures. *Reports Prog. Phys.* **2008**, *71*.

(13)   Xu, X. L.; Chen, Z. H.; Li, Y.; Chen, W. K.; Li, J. Q. Bulk and Surface Properties of Spinel Co3O4 by Density Functional Calculations. *Surf. Sci.* **2009**, *603*, 653–658.

(14)   Montoya, A.; Haynes, B. S. Periodic Density Functional Study of Co3O4 Surfaces. *Chem. Phys. Lett.* **2011**, *502*, 63–68.

(15)   Xie, Y.; Guo, H. Thermodynamic Stability of Cobalt Oxide's Low-Index Surfaces from Density Functional Theory Calculations. *Surf. Coatings Technol.* **2017**, *320*, 18–22.

(16)   Busca, G.; Guidetti, R.; Lorenzelli, V. Fourier-Transform Infrared Study of the Surface Properties of Cobalt Oxides. *J. Chem. Soc. Faraday Trans* **1990**, *86*, 989–994.

(17)   Chuang, T. J.; Brundle, C. R.; Rice, D. W. Interpretation of the X-Ray Photoemission Spectra of Cobalt Oxides and Cobalt Oxide Surfaces. *Surf. Sci.* **1976**, *59*, 413–429.

(18)   Faisal, F.; Bertram, M.; Stumm, C.; Cherevko, S.; Geiger, S.; Kasian, O.; Lykhach, Y.; Lytken, O.; Mayrhofer, K. J. J.; Brummel, O.; Libuda, J. Atomically Defined Co3O4(111) Thin Films Prepared in Ultrahigh Vacuum: Stability under Electrochemical Conditions. *J.*

Phys. Chem. C **2018**, *122*, 7236–7248.

(19) Nguyen, L.; Zhang, S.; Yoon, S. J.; Tao, F. F. Preferential Oxidation of CO in H 2 on Pure Co3O4−x and Pt/Co3O4−x. *ChemCatChem* **2015**, *7*, 2346–2353.

(20) Lukashuk, L.; Yigit, N.; Rameshan, R.; Kolar, E.; Teschner, D.; Hävecker, M.; Knop-Gericke, A.; Schlögl, R.; Föttinger, K.; Rupprechter, G. Operando Insights into CO Oxidation on Cobalt Oxide Catalysts by NAP-XPS, FTIR, and XRD. *ACS Catal.* **2018**, *8*, 8630–8641.

(21) Petitto, S. C.; Marsh, E. M.; Carson, G. A.; Langell, M. A. Cobalt Oxide Surface Chemistry: The Interaction of CoO(1 0 0), Co3O4(1 1 0) and Co3O4(1 1 1) with Oxygen and Water. *J. Mol. Catal. A Chem.* **2008**, *281*, 49–58.

(22) Schwarz, M.; Faisal, F.; Mohr, S.; Hohner, C.; Werner, K.; Xu, T.; Skála, T.; Tsud, N.; Prince, K. C.; Matolín, V.; Lykhach, Y.; Libuda, J. Structure-Dependent Dissociation of Water on Cobalt Oxide. *J. Phys. Chem. Lett.* **2018**, 1–7.

(23) Schwarz, M.; Mohr, S.; Hohner, C.; Werner, K.; Xu, T.; Libuda, J. Water on Atomically-Defined Cobalt Oxide Surfaces Studied by Temperature-Programmed IR Reflection Absorption Spectroscopy and Steady State Isotopic Exchange. *J. Phys. Chem. C* **2018**, acs.jpcc.8b04611.

(24) Chen, J.; Selloni, A. Electronic States and Magnetic Structure at the Co3O4(110) Surface: A First-Principles Study. *Phys. Rev. B - Condens. Matter Mater. Phys.* **2012**, *85*, 1–9.

(25) Plaisance, C. P.; van Santen, R. A. Structure Sensitivity of the Oxygen Evolution Reaction Catalyzed by Cobalt (II, III) Oxide. *J. Am. Chem. Soc.* **2015**, *137*, 14660–14672.

(26) Selcuk, S.; Selloni, A. DFT+U Study of the Surface Structure and Stability of Co 3 O 4 (110): Dependence on U. *J. Phys. Chem. C* **2015**, *119*, 9973–9979.

(27) Lu, J.; Song, J. J.; Niu, H.; Pan, L.; Zhang, X.; Wang, L.; Zou, J. J. Periodic Density Functional Theory Study of Ethylene Hydrogenation over Co3O4(1 1 1) Surface: The Critical Role of Oxygen Vacancies. *Appl. Surf. Sci.* **2016**, *371*, 61–66.

(28) Zasada, F.; Piskorz, W.; Cristol, S.; Paul, J. F.; Kotarba, A.; Sojka, Z. Periodic DFT and Atomistic Thermodynamic Studies of Cobalt Spinel Nanocrystals in Wet Environment – Molecular Interpretation of Water Adsorption Equilibria. *J. Phys. Chem. C* **2010**, No. 100, 4–6.

(29) Jiang, D. E.; Dai, S. The Role of Low-Coordinate Oxygen on Co3O4(110) in Catalytic CO Oxidation. *Phys. Chem. Chem. Phys.* **2011**, *13*, 978–984.

(30) Kresse, G.; Hafner, J. Ab Initio Molecular Dynamics for Liquid Metals. *Phys. Rev. B* **1993**, *47*, 558–561.

(31) Kresse, G.; Furthmüller, J. Efficiency of Ab-Initio Total Energy Calculations for Metals and Semiconductors Using a Plane-Wave Basis Set. *Comput. Mater. Sci.* **1996**, *6*, 15–50.

(32) Kresse, G.; Furthmüller, J. Efficient Iterative Schemes for Ab Initio Total-Energy Calculations Using a Plane-Wave Basis Set. *Phys. Rev. B - Condens. Matter Mater. Phys.* **1996**, *54*, 11169–11186.

(33) Perdew, J. P.; Burke, K.; Ernzerhof, M. Generalized Gradient Approximation Made Simple. *Phys. Rev. Lett.* **1996**, *77*, 3865–3868.

(34) Steinmann, S. N.; Corminboeuf, C. A Generalized-Gradient Approximation Exchange Hole Model for Dispersion Coefficients. *J. Chem. Phys.* **2011**, *134*.

(35) Steinmann, S. N.; Corminboeuf, C. Comprehensive Benchmarking of a Density-Dependent Dispersion Correction. *J. Chem. Theory Comput.* **2011**, *7*, 3567–3577.

(36) Joubert, D. From Ultrasoft Pseudopotentials to the Projector Augmented-Wave Method.

Phys. Rev. B - Condens. Matter Mater. Phys. **1999**, *59*, 1758–1775.

(37)   Dudarev, S.; Botton, G. Electron-Energy-Loss Spectra and the Structural Stability of Nickel Oxide: An LSDA+U Study. *Phys. Rev. B - Condens. Matter Mater. Phys.* **1998**, *57*, 1505–1509.

(38)   Wang, L.; Maxisch, T.; Ceder, G. Oxidation Energies of Transition Metal Oxides within the GGA+U Framework. *Phys. Rev. B - Condens. Matter Mater. Phys.* **2006**, *73*, 1–6.

(39)   Heyd, J.; Scuseria, G. E.; Ernzerhof, M. Hybrid Functionals Based on a Screened Coulomb Potential. *J. Chem. Phys.* **2003**, *118*, 8207.

(40)   Heyd, J.; Scuseria, G. E.; Ernzerhof, M. Erratum: "Hybrid Functionals Based on a Screened Coulomb Potential" [J. Chem. Phys. 118, 8207 (2003)]. *J. Chem. Phys.* **2006**, *124*, 219906.

(41)   Allen, J. P.; Watson, G. W. Occupation Matrix Control of D- and f-Electron Localisations Using DFT + U. *Phys. Chem. Chem. Phys.* **2014**, *16*, 21016–21031.

(42)   Reuter, K.; Scheffler, M. Composition, Structure, and Stability of RuO 2 (110) as a Function of Oxygen Pressure. *Phys. Rev. B* **2001**, *65*, 035406.

(43)   Reuter, K.; Scheffler, M. Composition and Structure of the RuO2(110) Surface in an O2 and CO Environment: Implications for the Catalytic Formation of CO2. *Phys. Rev. B* **2003**, *68*, 045407.

(44)   Pack, J. D.; Monkhorst, H. J. "Special Points for Brillouin-Zone Integrations"-a Reply. *Phys. Rev. B* **1977**, *16*, 1748–1749.

(45)   Momma, K.; Izumi, F. VESTA: A Three-Dimensional Visualization System for Electronic and Structural Analysis. *J. Appl. Crystallogr.* **2008**, *41*, 653–658.

(46)   Dementyev, P.; Dostert, K.-H.; Ivars-Barceló, F.; O'Brien, C. P.; Mirabella, F.; Schauermann, S.; Li, X.; Paier, J.; Sauer, J.; Freund, H.-J. Water Interaction with Iron Oxides. *Angew. Chemie Int. Ed.* **2015**, *54*, 13942–13946.

(47)   Liu, X.; Prewitt, C. T. High-Temperature X-Ray Diffraction Study of Co3O4: Transition from Normal to Disordered Spinel. *Phys. Chem. Miner.* **1990**, *17*, 168–172.

(48)   Zasada, F.; Gryboś, J.; Piskorz, W.; Sojka, Z. Cobalt Spinel (111) Facets of Various Stoichiometry - DFT+U and Ab Initio Thermodynamic Investigations. *J. Phys. Chem. C* **2018**, *122*, 2866–2879.

(49)   Yan, G.; Wahler, T.; Schuster, R.; Schwarz, M.; Hohner, C.; Werner, K.; Libuda, J.; Sautet, P. Water on Oxide Surfaces: A Triaqua Surface Coordination Complex on Co3O4(111). *J. Am. Chem. Soc.* **2019**, *141*, 5623–5627.

(50)   Capdevila-Cortada, M.; Łodziana, Z.; López, N. Performance of DFT+U Approaches in the Study of Catalytic Materials. *ACS Catal.* **2016**, *6*, 8370–8379.

(51)   Chen, J.; Selloni, A. First Principles Study of Cobalt (Hydr)Oxides under Electrochemical Conditions. *J. Phys. Chem. C* **2013**, *117*, 20002–20006.

(52)   Bajdich, M.; García-Mota, M.; Vojvodic, A.; Nørskov, J. K.; Bell, A. T. Theoretical Investigation of the Activity of Cobalt Oxides for the Electrochemical Oxidation of Water. *J. Am. Chem. Soc.* **2013**, *135*, 13521–13530.

(53)   Hu, W.; Cao, X.-M.; Hu, P. DFT+ U Study on Catalysis by Co 3 O 4 : Influence of U Value and a Surface-Bulk Bi-U Strategy. *J. Phys. Chem. C* **2018**, *122*, 19593–19602.

(54)   Xie, X.; Li, Y.; Liu, Z. Q.; Haruta, M.; Shen, W. Low-Temperature Oxidation of CO Catalysed by Co 3 O 4 Nanorods. *Nature* **2009**, *458*, 746–749.

(55)   Grillo, F.; Natile, M. M.; Glisenti, A. Low Temperature Oxidation of Carbon Monoxide: The Influence of Water and Oxygen on the Reactivity of a Co3O4 Powder Surface. *Appl.*

Catal. B Environ. **2004**, *48*, 267–274.

(56) Finocchio, E.; Busca, G.; Lorenzelli, V.; Escribano, V. S. FTIR Studies on the Selective Oxidation and Combustion of Light Hydrocarbons at Metal Oxide Surfaces, Part 2: Propane and Propene Oxidation on Co3O4. *J. Chem. Soc. Faraday Trans.* **1996**, *92*, 1587.

(57) Tang, X.; Li, J.; Hao, J. Synthesis and Characterization of Spinel Co3O4 Octahedra Enclosed by the {1 1 1} Facets. *Mater. Res. Bull.* **2008**, *43*, 2912–2918.

(58) Russo, N.; Fino, D.; Saracco, G.; Specchia, V. N2O Catalytic Decomposition over Various Spinel-Type Oxides. *Catal. Today* **2007**, *119*, 228–232.

(59) Piskorz, W.; Zasada, F.; Stelmachowski, P.; Kotarba, A.; Sojka, Z. Decomposition of N2O over the Surface of Cobalt Spinel: A DFT Account of Reactivity Experiments. *Catal. Today* **2008**, *137*, 418–422.

(60) Zhang, S.; Nguyen, L.; Liang, J. X.; Shan, J.; Liu, J. J.; Frenkel, A. I.; Patlolla, A.; Huang, W.; Li, J.; Tao, F. F. Catalysis on Singly Dispersed Bimetallic Sites. *Nat. Commun.* **2015**, *6*, 1–10.

(61) Fung, V.; Tao, F. F.; Jiang, D. Trends of Alkane Activation on Doped Cobalt (II, III) Oxide from First Principles. *ChemCatChem* **2017**, *10*, 244–249.

(62) Tang, Y.; Ma, L.; Dou, J.; Andolina, C. M.; Li, Y.; Ma, H.; House, S. D.; Zhang, X.; Yang, J.; Tao, F. Transition of Surface Phase of Cobalt Oxide during CO Oxidation. *Phys. Chem. Chem. Phys.* **2018**, *20*, 6440–6449.

(63) Zasada, F.; Janas, J.; Piskorz, W.; Gorczyn, M.; Sojka, Z. Total Oxidation of Lean Methane over Cobalt Spinel Nanocubes Controlled by the Self-Adjusted Redox State of the Catalyst: Experimental and Theoretical Account for Interplay between the Langmuir − Hinshelwood and Mars − Van Krevelen Mechanisms. *ACS Catal.* **2017**, *7*, 2853−2867.

(64) Ferstl, P.; Mehl, S.; Arman, M. A.; Schuler, M.; Toghan, A.; Laszlo, B.; Lykhach, Y.; Brummel, O.; Lundgren, E.; Knudsen, J.; Hammer, L.; Schneider, M. A.; Libuda, J. Adsorption and Activation of CO on Co $_3$ O $_4$ (111) Thin Films. *J. Phys. Chem. C* **2015**, *119*, 16688–16699.

(65) Pang, X. Y.; Liu, C.; Li, D. C.; Lv, C. Q.; Wang, G. C. Structure Sensitivity of CO Oxidation on Co3O4: A DFT Study. *ChemPhysChem* **2013**, *14*, 204–212.

(66) Hu, C. H.; Chizallet, C.; Mager-Maury, C.; Corral-Valero, M.; Sautet, P.; Toulhoat, H.; Raybaud, P. Modulation of Catalyst Particle Structure upon Support Hydroxylation: Ab Initio Insights into Pd13 and Pt13/γ-Al 2O3. *J. Catal.* **2010**, *274*, 99–110.

(67) Towns, J.; Cockerill, T.; Dahan, M.; Foster, I.; Gaither, K.; Grimshaw, A.; Hazlewood, V.; Lathrop, S.; Lifka, D.; Peterson, G. D.; Roskies, R.; Scott, J. R.; Wilkens-Diehr, N. XSEDE: Accelerating Scientific Discovery. *Comput. Sci. Eng.* **2014**, *16*, 62–74.

(68) Nystrom, N. A.; Levine, M. J.; Roskies, R. Z.; Scott, J. R. Bridges: A Uniquely Flexible HPC Resource for New Communities and Data Analytics. In *Proceedings of the 2015 XSEDE Conference: Scientific Advancements Enabled by Enhanced Cyberinfrastructure*; ACM: St. Louis, Missouri, 2015; p 30.

TOC graphic:

423 K
Reductive

<300 K
Oxidative

Co$_3$O$_4$(111)

423 K
Oxidative

873 K
Oxidative